J. Fluid Mech. (2013), *vol.* 722, *pp.* 121–158. © Cambridge University Press 2013
doi:10.1017/jfm.2013.53

Rigid ring-shaped particles that align in simple shear flow

Vikram Singh[1], Donald L. Koch[1,†] and Abraham D. Stroock[1,2]

[1]Department of Chemical and Biomolecular Engineering, Cornell University, Ithaca, NY 14853, USA
[2]Kavli Institute of Cornell, Cornell University, Ithaca, NY 14853, USA

(Received 8 August 2012; revised 9 January 2013; accepted 21 January 2013;
first published online 28 March 2013)

Most rigid, torque-free, low-Reynolds-number, axisymmetric particles undergo a time-periodic tumbling motion in a simple shear flow, with their axes of symmetry following a set of closed Jeffery orbits. We have identified a class of rigid, ring-like particles whose axes of symmetry instead reach a permanent alignment near the velocity gradient direction with the plane of the particle aligning near the flow–vorticity plane. An asymptotic analysis for small particle aspect ratio (ratio of length parallel to the axis of symmetry to diameter perpendicular to the axis) shows that an appropriate asymmetry of the ring cross-section with a thinner outer edge and thicker inner edge leads to a tendency to rotate in a direction opposite to the vorticity; this tendency can balance the usual rotation rate associated with the finite thickness of the particle. Boundary integral computations for finite particle aspect ratios are used to determine the conditions of aspect ratio and degree of asymmetry that lead to the aligning behaviour and the final orientation of the axis of symmetry of the aligned particles. The aligning particle follows an equation of motion similar to the Leslie–Erickson equation for the director of a small-molecule nematic liquid crystal. However, whereas the alignment of the director arises from intermolecular interactions, the ring-like particle aligns solely due to its intrinsic rotational motion in a low-Reynolds-number flow.

Key words: boundary integral methods, low-Reynolds-number flows, suspensions

1. Introduction

It is well known that most rigid particles rotate continuously in simple shear flow of a Newtonian fluid in the absence of inertial effects. A natural question to ask is whether there are any exceptional particle shapes which can allow the particle to stop rotating and reach a permanent alignment. This question was first raised in Bretherton's classical paper (Bretherton 1962*a*) on the rotation of axisymmetric particles. Bretherton argued that a dumbbell consisting of asymmetrical beads could stop rotating but he concluded that the aspect ratio of the connecting rod required to achieve this behaviour was unrealistically large so that a rigid particle of this shape could not be created in practice. Inspired by Bretherton's work, we show that moderate-aspect-ratio ring-shaped particles with a local cross-sectional shape that is thinner on the outer edge than on the inner edge can align in a simple shear flow. The

† Email addresses for correspondence: dlk15@cornell.edu, vs225@cornell.edu

https://doi.org/10.1017/jfm.2013.53 Published online by Cambridge University Press

asymmetry of the shape leads to a force per unit circumference that opposes the usual rotation of a finite-aspect-ratio particle with the fluid vorticity.

Understanding the motion of a single particle in flow is a fundamental problem of fluid mechanics with implications in a wide variety of fields like engineering, geophysics, and physiology (Bhattacharyya 1966; Gay 1967; Leal 1980; Chien 1987; Goldsmith 1993; Edwards *et al.* 1997). Stokes (1851) was the first to analyse the translational motion of a rigid sphere in an unbounded quiescent fluid at low Reynolds number. Einstein (1906) later studied the behaviour of a single spherical particle in simple shear flow to estimate the effective viscosity of a dilute suspension of spherical particles. The behaviour of particles with non-spherical shapes in simple shear flow at low Reynolds number was first studied by Jeffery (1922). Jeffery showed that in the absence of inertial effects, a spheroidal (ellipsoid with two equal semi-diameters) particle centre translates with the velocity of the fluid and the axis of symmetry rotates in a periodic motion with a period that depends on the aspect ratio (κ) of the particle where κ is defined as the ratio of length (L) parallel to the axis of symmetry to diameter (d) perpendicular to the axis. In this Jeffery rotational motion, the time period of particle rotation increases as the aspect ratio becomes large or small and the particle spends more time aligned with its longer axis in the flow direction. However, to date, it has been thought that there is no shape for which a rigid particle completely stops rotating in simple shear flow at finite aspect ratio.

While no previous studies have revealed a rigid particle that stops rotating in unbounded simple shear flow of a low-Reynolds-number Newtonian fluid, there are a number of other conditions in which particles can align in simple shear flow. Deformable particles like vesicles with fluid or solid inclusions (Kantsler & Steinberg 2005; Deschamps, Kantsler & Steinberg 2009; K Veerapaneni *et al.* 2011), droplets (Torza, Cox & Mason 1972), and the swimming micro-organism chlamydomonas (Rafai, Jibuti & Peyla 2010) can align in simple shear flow. Particles can also align in simple shear flow due to inertial effects as shown by Subramanian & Koch (2005). A fibre has also been observed to align in a viscoelastic fluid (Iso, Koch & Cohen 1996). Interactions with the wall can also stop a particle from tumbling at separations smaller than a critical value as revealed for oblate spheroidal particles by the simulations of Mody & King (2005).

Rigid particles in low-Reynolds-number flows can also align in linear flows other than simple shear flow. In particular, a two-dimensional linear flow in which the magnitude of the extension rate exceeds the magnitude of the rotation rate by a sufficient (aspect ratio dependent) factor will cause a particle to stop rotating (Ghosh & Ramberg 1976). In a pure extensional flow, a particle aligns with its long axis along the axis of extension. For the case of simple shear flow where the magnitudes of the extensional and rotational flows are equal no such alignment has been achieved. Linear flows are of particular interest because suspended particles are often much smaller than the scale of the fluid flow. Under these circumstances, one can Taylor expand the fluid velocity near the particle. The leading-order uniform flow causes only a translational motion of a neutrally buoyant particle, while the linear flow is the first component to cause particle rotation. Simple shear flow is the linear flow of greatest interest because it represents the local linear flow for a unidirectional fluid flow. In a steady unidirectional fluid flow, the velocity gradient is independent of time along the particle trajectory so that the particle can experience the shear long enough to reach its final oscillatory or aligning behaviour. While one can observe a steady two-dimensional fluid flow (for instance, extensional flow) in the particle frame by controlling its position to remain at the stagnation point of a four-roll mill flow, the local linear flow

https://doi.org/10.1017/jfm.2013.53 Published online by Cambridge University Press

in the particle reference frame will generally be unsteady in other non-unidirectional fluid flows.

The original work of Jeffery described the motion of spheroidal particles in terms of the aspect ratio of the particle. Bretherton (1962*a*) later showed that all axisymmetric particles follow Jeffery's equation of motion for spheroidal particles in simple shear flow as long as a tumbling parameter (λ) or an effective aspect ratio (κ_e) is used in the equation for the rotation rate. At low Reynolds number, Bretherton (Jeffery 1922; Bretherton 1962*a*) showed that the rotational motion of an axisymmetric particle in linear flow is given by:

$$\dot{\boldsymbol{p}} = \boldsymbol{p} \cdot \boldsymbol{\Omega} + \lambda(\boldsymbol{p} \cdot \boldsymbol{E} - \boldsymbol{ppp} : \boldsymbol{E}), \tag{1.1}$$

where $\boldsymbol{p}$ is the orientation of the axis of symmetry of the particle, $\dot{\boldsymbol{p}}$ is the rate of change of the orientation, and λ is a constant which depends on the shape of the particle. Motion of the normal director vector of a liquid crystal in a linear flow can also be described using (1.1) when the deviation from equilibrium is small as is most often the case for small-molecule liquid crystals (Larson 1991; Chen & Koch 1997). In such systems, molecular interactions lead to the alignment and either $\lambda > 1$ (flow aligning liquid crystals) or $\lambda < 1$ (tumbling liquid crystals) can be achieved depending on the intermolecular potentials. For the case of liquid crystals, λ is called the tumbling parameter and $\boldsymbol{p}$ is the orientation of the normal director vector. In this work also we will refer to λ as the tumbling parameter where $\boldsymbol{p}$ will be the orientation of the particle axis of symmetry. For a spheroid, $\lambda = (\kappa^2 - 1)/(\kappa^2 + 1)$ where κ is the actual aspect ratio of the particle. For the other shapes that are known to date $|\lambda| \leqslant 1$ and one can replace κ by an effective aspect ratio, κ_e, which will in general be different from the actual particle aspect ratio (Bretherton 1962*a*). In (1.1), $\boldsymbol{\Omega}$ is the vorticity tensor and $\boldsymbol{E}$ is the strain tensor, given by:

$$\boldsymbol{E} = \tfrac{1}{2}(\nabla \boldsymbol{v} + \nabla \boldsymbol{v}^T), \tag{1.2}$$

$$\boldsymbol{\Omega} = \tfrac{1}{2}(\nabla \boldsymbol{v} - \nabla \boldsymbol{v}^T). \tag{1.3}$$

For simple shear flow, the time period of rotation, T, of a particle with $-1 \leqslant \lambda \leqslant 1$ is given by:

$$T = \frac{2\pi}{\gamma(1 - \lambda^2)}, \tag{1.4}$$

where γ is the shear rate. For $-1 < \lambda < 1$, the period of rotation of the particle is finite, and κ lies between 0 and ∞. In the asymptotic limit, the particle aligns with its longer axis in the flow direction for $\lambda = 1$ or $\lambda = -1$, which corresponds to an aspect ratio of $\kappa = \infty$ (infinitesimally thin rod) or $\kappa = 0$ (infinitesimally thin disk) respectively for a spheroid. Both these shapes, a line and a plane, are obviously only mathematical possibilities. It should be noted that in the microhydrodynamics literature where particles encountered generally have $|\lambda| < 1$, κ_e is generally used to describe the behaviour of a particle but for a value of $|\lambda| \geqslant 1$, κ_e corresponds to an imaginary value. Since in this work we encounter particle shapes for which $|\lambda| > 1$, we use the tumbling parameter to describe the behaviour of the particles studied here.

The forces which act to rotate a typical particle such as a spheroid in simple shear flow are shown in figure 1(*a*). The net torque due to the combination of these forces rotates the particle in the vorticity direction. Although the forces in the y-direction retard the rotation of the particle they always lead to a smaller torque than the forces in the x-direction for spheroidal particles. Cox (1971) and Singh *et al.* (2013) have

https://doi.org/10.1017/jfm.2013.53 Published online by Cambridge University Press

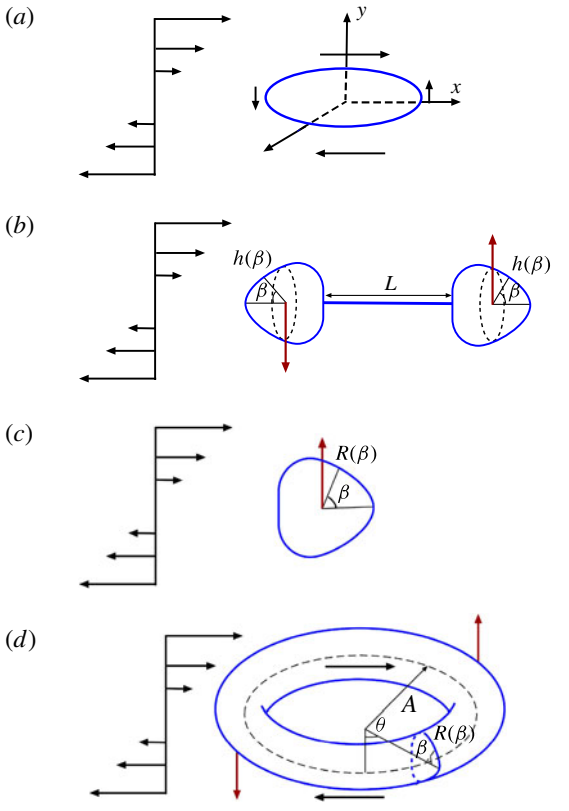


FIGURE 1. (Colour online) Schematic representation of forces acting on non-spherical rigid particles in simple shear flow. (*a*) Typical forces acting on a spheroid causing it to rotate. (*b*) Bretherton's proposal for a particle shape that could align in simple shear flow. The axis of symmetry of the particle aligns near the flow direction. (*c*) Schematic of a lateral force acting on a perturbed circle. (*d*) Schematic of forces acting on a ring. Forces due to asymmetry in the shape generate a torque in the direction opposite to the vorticity.

performed asymptotic analyses to calculate the rotation rates for a variety of shapes at high and low aspect ratio, respectively, in simple shear flow and found that for the classes of shapes studied, the rotational motion does not cease until the aspect ratio is ∞ or 0.

Bretherton (1962*a*) in his classic paper describing the motion of axisymmetric particles, presented one possible particle shape with $\lambda \geqslant 1$, such that it would stop rotating in simple shear flow. Bretherton's shape (figure 1*b*) included two almost spherical particles connected by a thin rod of length, L and diameter, d. The shape of the almost spherical particles is given by:

$$h(\beta) = g(1 + \alpha P_3(\cos\beta)). \tag{1.5}$$

Here h is the distance of the surface from the centre of the deformed sphere, g is the radius of the undeformed sphere, β is the angle between the radial vector on the surface and the rod connecting the two deformed spheres, P_3 is the third Legendre polynomial, and α is a small parameter. On this assembly of particles, there are three types of torque acting: (i) a torque acting in the vorticity direction on the particle

https://doi.org/10.1017/jfm.2013.53 Published online by Cambridge University Press

when the almost spherical particles at the end are not allowed to rotate due to the connecting rod; (ii) another torque in the vorticity direction on the thin connecting rod; and (iii) a torque in a direction opposite to vorticity which originates from lateral forces (figure 1*b*) acting on particles due to their lack of spherical symmetry. Here, the first two are the typical torques that act on particles in simple shear flow. The opposing torque acting on the fore–aft asymmetric particles is less familiar, although a number of authors (Brenner 1964; Nir & Acrivos 1973) have noted the existence of lateral forces on non-fore–aft symmetric particles in other contexts. Solving Stokes equation around the almost spherical particles, Bretherton calculated that in the limit when the torque acting on the rod connecting the particles is infinitesimal (i.e. neglecting torque (ii)), a distance, $L = 28g/3\alpha$ between the two almost spherical particles will stop the entire assembly of the particles from rotating. Bretherton estimated that the torque on the thin rod can be neglected if $1/\ln(L/d) \ll \alpha$. For a value of $\alpha = 0.1$, this would mean that the aspect ratio ($\kappa = L/d$) of the rod should be much greater than e^{10}. Since the resistance of an elastic beam to bending decreases rapidly with increasing aspect ratio, from a practical standpoint a rigid particle with such an aspect ratio would not be possible. Forgacs & Mason (1959) suggested that in order for a fibre to avoid bending due to viscous stresses in shear flow, its elastic modulus should be larger than $2\mu\gamma\kappa^4/(\ln(2\kappa) - 1.75)$, and this, for a fluid of viscosity, $\mu = 1$ cP, shear rate, $\gamma = 1\ \mathrm{s}^{-1}$, and $\kappa = e^{10}$ turns out to be 5.3×10^4 GPa which is $\sim$50 times larger than the elastic modulus of diamond. Bretherton referred to these shapes as extreme and concluded by saying that 'in the private guess of the author the thickness of the thin rod must be too small to be consistent with rigidity'.

Since Bretherton's work, we know of no report of a particle shape that aligns in simple shear flow, although the problem has been mentioned in some classical texts (Kim & Karilla 1991; Larson 1999). The particular challenge in determining the shape of the particle for which $|\lambda| \geqslant 1$ is that there is no explicit relation between the shape of a particle and λ, even though λ depends only on the particle shape and is independent of the flow. For a general particle shape, an appropriate Stokes flow problem needs to be solved to relate the angular velocity of the particle with the strain rate (1.1) to determine the unknown parameter λ (Batchelor 1970; Cox 1971). We note one attempt by Willis (1977) to develop a model in which the rotational motion of the particle can be described explicitly based on the shape of the body without solving the full fluid mechanics problem. Willis' model is based on the *ad hoc* assumption that the torque on a particle is proportional to the integral over the particle volume of the cross-product of the position relative to the particle centre and the relative velocity between the particle and the undisturbed fluid velocity. In Willis' model, the three principal moments of inertia (without the density factors) of the body could be used to calculate the value of λ. Despite the non-rigorous assumptions in Willis' model, it was very successful in describing the rotation rate of a variety of shapes. This model predicted that there cannot be any axisymmetric particle shape for which $|\lambda| \geqslant 1$, so the model would be qualitatively inaccurate for particles that can align in simple shear flow.

In this work, we present finite-aspect-ratio ring-shaped rigid particles (figure 1*d*) which can stop tumbling in simple shear flow at low Reynolds number. The non-tumbling ring shapes can be obtained by revolving a two-dimensional shape lacking fore–aft symmetry (figure 1*c*) about an axis as shown in figure 1(*d*). The asymmetric shape of the cross-section is a circular shape perturbed with a third Fourier mode analogous to Bretherton's nearly spherical shape. Unlike Bretherton's non-tumbling particle shape where the torque acting on the connecting rod in the vorticity direction

https://doi.org/10.1017/jfm.2013.53 Published online by Cambridge University Press

was large enough to rotate the particle, the ring shapes introduced here do not require a connecting rod and hence there is no additional torque in the vorticity direction due to it. Instead the ring shape provides the necessary connectivity and the asymmetric shape creates a lateral force per unit circumference at all angular positions opposing rotation with vorticity. In the next section, we discuss the motion that a particle with $|\lambda| \geqslant 1$ follows before aligning as well as determining the final orientation as a function of λ. In § 3, we present an asymptotic analysis for the rotation of a thin ring-shaped particle with an asymmetric cross-section. We show how certain types of asymmetry in cross-sectional shape can give rise to rotational motion in a direction opposite to the direction of vorticity. We discuss some of the basic characteristics of the shape that can lead to the non-tumbling behaviour of the particle. We show that lack of fore–aft symmetry in the local cross-section of the ring is a necessary but not sufficient condition for the alignment of the ring-shaped particles. In § 4, we describe the boundary element method and the details of the method pertinent to the present problem. We then present boundary element simulation predictions at finite aspect ratio. We determine the largest aspect ratio at which the asymmetric ring can remain aligned for different degrees of asymmetry. We also estimate the angle with respect to the flow at which the particle will align as a function of its shape. Finally, we discuss some of the implications of alignment for the properties of suspensions of these particles.

2. Motion of a particle with $|\lambda| \geqslant 1$

Bretherton (1962*a*) described the motion that a particle with $|\lambda| \geqslant 1$ would undergo before it stops rotating; we reproduce his results in this section using a slightly different notation that is closer to that of Jeffery. Unlike Jeffery's rotating particles ($|\lambda| \leqslant 1$), which rotate in a periodic motion in one of an infinite set of orbits, particles with $|\lambda| \geqslant 1$ align in one of two stable equilibrium directions (figure 2). The equations for the rotational motion can be obtained by solving (1.1) and are given by:

$$\tan\phi = \begin{cases} p' \tanh\xi & \text{for } C_1 < 0 \\ \dfrac{p'}{\tanh\xi} & \text{for } C_1 > 0, \end{cases} \tag{2.1}$$

$$\tan\theta = \begin{cases} C\left((p'^2+1)\cosh 2\xi - p'^2 + 1\right)^{1/2} & \text{for } C_1 < 0 \\ C\left((p'^2+1)\cosh 2\xi + p'^2 - 1\right)^{1/2} & \text{for } C_1 > 0, \end{cases} \tag{2.2}$$

where $p' = ((\lambda+1)/(\lambda-1))^{1/2}$ $(= -\mathrm{i}\kappa_e)$, $\xi = (p't/p'^2 - 1) - \ln|C_1|/2$, ϕ_0 and θ_0 are the orientation angles of the particle at $t = 0$, $C_1 = (\tan\phi_0 - p')/(\tan\phi_0 + p')$ is a constant that depends on the initial orientation (ϕ_0), and C is the orbit constant of the particle trajectory which is also determined by the initial orientation of the particle (ϕ_0, θ_0). Here we have followed Jeffery's convention and adopted a spherical coordinate system with θ as the angle of the particle orientation relative to the vorticity (z-axis) direction and ϕ as the angle of the projection of the particle orientation into the flow–gradient plane relative to the gradient (y-axis) direction. The orbit constant, C, is analogous to the orbit constant used to describe Jeffery's rotational motion. The other constant of integration, C_1, depends only on the projection of the initial orientation into the flow–gradient plane.

As $\gamma t \to \infty$, irrespective of the initial orientation (except for the four unstable equilibrium points), the orientation of the particle approaches one of the two stable

https://doi.org/10.1017/jfm.2013.53 Published online by Cambridge University Press

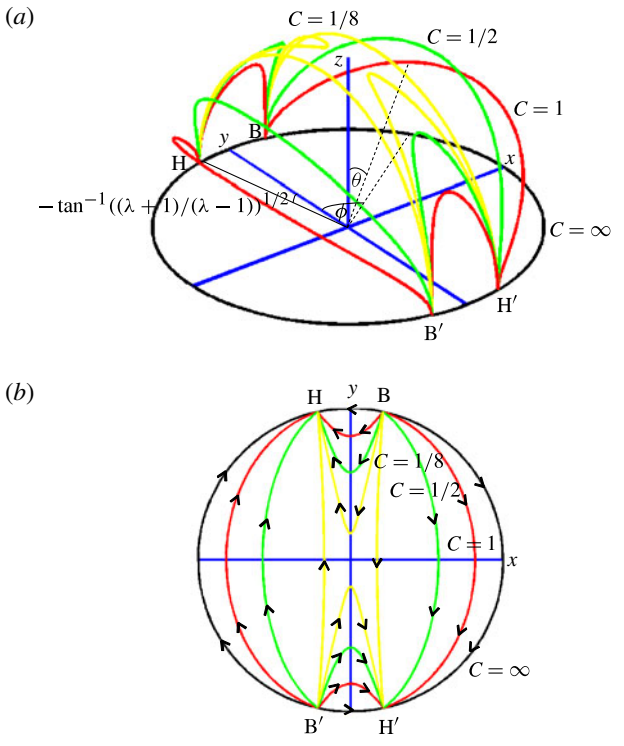


FIGURE 2. (Colour online) Motion of particles that align in simple shear flow. (*a*) Trajectories of a particle with different initial conditions in simple shear flow for $\lambda = -1.1$. (*b*) Projections of the same trajectories in the x–y-plane. The trajectories represented here are for $C = \infty$ (black online), $C = 1$ (red online). $C = 1/2$ (green) and $C = 1/8$ (yellow online). Here, H and H$'$ correspond to stable equilibrium positions and B and B$'$ to unstable equilibrium positions.

orientations, given by $\theta = \pi/2$ and

$$\tan\phi = \begin{cases} p' & \text{for } \lambda \geqslant 1 \\ -p' & \text{for } \lambda \leqslant -1. \end{cases} \tag{2.3}$$

For $\lambda = 1$, $p' = \infty$ and for $\lambda = -1$, $p' = 0$ so that in both these cases the long axis of the particle is aligned in the flow direction. As the magnitude of λ increases, the inclination of the long axis of the particle to the flow–vorticity plane approaches a limiting value of $\pi/4$ which is the principal direction of the extensional component of the flow. This maximum inclination of the long axis to the flow direction is achieved when $\lambda \to \pm\infty$. When $|\lambda + 1| \ll 1$, the angle of the stable orientation of the particle to the shear gradient direction is given by $-((1+\lambda)/-2)^{1/2}$.

Figure 2(*a*) shows trajectories of the particle axis of symmetry for different values of the orbit constant for $\lambda = -1.1$. Figure 2(*b*) shows projections of the trajectories of the particle in the flow–gradient plane. Points H and H$'$ are the points of stable equilibrium where the typical torque due to the shear flow cancels the torque due to the asymmetric shape. Apart from the two stable orientations in the flow–gradient plane there are also two unstable orientations in this plane given by points B and B$'$ in figure 2. A small perturbation from these two unstable equilibrium positions will

https://doi.org/10.1017/jfm.2013.53 Published online by Cambridge University Press

move the particle towards one of the two stable equilibrium positions. There are two additional unstable equilibrium positions in which the particle can stay aligned, along the $\pm z$ (vorticity) direction. In these orientations, in the absence of any perturbations, the particle could continue rotating about its axis without ever aligning. Again, a small perturbation out of the vorticity direction would cause the particle to drift towards the stable orientations H or H′. In the case considered here where the particle has a mirror symmetry about the plane perpendicular to the axis of symmetry (example in figure 1*d*), the two stable equilibria H and H′ are indistinguishable. Similarly, there are two indistinguishable pairs of unstable equilibria (B and B′ and $\pm z$). We note here that the aligning behaviour of the particle is consistent with Stokes flow reversibility. To see that this is true, we simply reverse the sign of the undisturbed simple shear flow at infinity. If the particle is initially aligned in the stable (H or H′) or unstable (B or B′) equilibrium directions, in the reverse flow also it will stay aligned except now it will be in the unstable (B or B′) or stable (H or H′) equilibrium directions. If the particle is initially flipping, in the reverse flow its angular velocity will simply reverse its sign while the particle will stay in the same orbit. Typically, a particle will approach a stable orientation during the forward shear flow. When the flow is reversed, this fixed point becomes unstable and the particle will undergo a flip to align with the newly stable fixed point which was the unstable fixed point of the forward shear flow.

In general, when a particle undergoes rotational motion in simple shear flow, the minimum angular velocity acting on the particle is observed when the long axis of the particle is aligned in the flow direction. In this case, the long axis of the particle is along the axis of symmetry for $\lambda > 0$ and perpendicular to the axis of symmetry for $\lambda < 0$. At the point of transition from tumbling to the non-tumbling state ($|\lambda| = 1$), the angular velocity of the particle is 0 with the long axis in the flow direction. A very simple test of the ability of a particle shape to avoid tumbling is thus that the angular velocity of the particle when oriented with its long axis along the flow direction is either 0 or in the direction opposite to the vorticity. Based on this simple idea, in the next section we use asymptotic analysis to introduce a particle shape which can stop rotating in simple shear flow. We establish that the particle stops tumbling by showing that the angular velocity of the particle with its long axis aligned in the flow direction becomes 0 which corresponds to $\lambda = -1$ for the shape considered here.

3. Asymptotic analysis for a thin ring with a slightly asymmetric cross-section

Like any incompressible linear flow, simple shear flow can be decomposed into an extensional flow and a rotational flow. In simple shear flow, the tendency of a particle to undergo rotational motion in the vorticity direction can be attributed to the rotational component of the shear flow. The rotational component of the flow tends to rotate the particle in the vorticity direction while the extensional component tends to align the long axis of the particle along the extensional axis. A rigid particle rotates with the rotational velocity of the fluid since the rotational component of the flow does not try to deform the particle. On the other hand, the response of a particle to the extensional flow component depends on its shape; for an axisymmetric particle the response can be completely described using λ, the tumbling parameter. In simple shear flow the strengths of the rotational and extensional components of the flow are equal and the response of the particle to the flow is dominated by the rotational component for $|\lambda| < 1$ and by the extensional component for $|\lambda| > 1$. As a result, the particle continues to rotate for $|\lambda| < 1$ and aligns for $|\lambda| \geqslant 1$.

https://doi.org/10.1017/jfm.2013.53 Published online by Cambridge University Press

In a linear flow at low Reynolds number in the absence of external forces, the centre of a particle with fore–aft symmetry translates with the fluid velocity. However, a particle without fore–aft symmetry can undergo a cross-stream migration due to the extensional component of the flow in the direction of shear. This phenomenon has been discussed in a number of studies (Bretherton 1962*a*; Brenner 1964; Nir & Acrivos 1973) for three-dimensional asymmetric particles of different shapes. Since the velocity of the particle must be a linear function of the rate-of-strain tensor and can also depend on the orientation vector, it must take the form

$$\boldsymbol{U} = \eta_1 \boldsymbol{E} \cdot \boldsymbol{p} + \eta_2 \boldsymbol{p}\boldsymbol{p} \cdot \boldsymbol{E} \cdot \boldsymbol{p} \tag{3.1}$$

where η_1 and η_2 are constants that depend on the particle shape. For a particle with fore–aft symmetry, the velocity of the particle when it is oriented in $\boldsymbol{p}$ and $-\boldsymbol{p}$ should be same, i.e. $\boldsymbol{U}(\boldsymbol{p}) = \boldsymbol{U}(-\boldsymbol{p})$. Hence, the coefficients $\eta_1 = \eta_2 = 0$ for such a particle and the particle translates with the fluid velocity. For a particle without fore–aft symmetry η_1 and η_2 can be non-zero. We will consider a particle with $\boldsymbol{p} = \boldsymbol{e}_x$ in a simple shear flow with $E_{xy} = E_{yx}$ as the only non-zero components of rate-of-strain tensor. Here $\boldsymbol{e}_x$ is the unit vector in the x-direction. In this case $U_x = 0$ and $U_y = \eta_1 E_{xy}$ and we will obtain a cross-stream drift velocity in the y-direction.

In this work, we show that a two-dimensional particle without fore–aft can also undergo such a cross-stream migration in simple shear flow (figure 1*c*). To the best of our knowledge, cross-stream migration of two-dimensional particles has not been discussed in the literature. Using such asymmetric shapes, we postulate that a three-dimensional axisymmetric shape (figure 1*d*) formed by revolving the two-dimensional cross-section (figure 1*c*) can align in simple shear flow. Using asymptotic analysis, we calculate the angular velocity generated by the local cross-sectional shape of the ring in terms of the degree of asymmetry (α) and aspect ratio of the particle. The condition of alignment is then obtained by balancing the angular velocity due to asymmetry with the angular velocity of the particle in the vorticity direction due to finite aspect ratio.

The cross-stream motion of the two-dimensional particle can be obtained through one of two approaches. First, one may directly pose the mobility problem of determining the relative velocity of the particle and fluid when the particle is force-free. Second, taking a resistivity approach, one may first compute the force acting on a particle held stationary in a simple shear flow and then compute the velocity of a particle relative to the fluid driven by this force. In addition to being more direct, the first, force-free approach has the advantage of avoiding Stokes paradox, which states that a Stokes fluid velocity cannot be determined in an unbounded two-dimensional flow with a net force acting on a particle. For this reason we adopt the first approach in our quantitative treatment of the cross-stream velocity of the two-dimensional particle and the resulting rotational velocity of the three-dimensional ring-shaped particle in § 3.2. However, the resistivity formulation has the advantage that one can more easily visualize the stresses driving the particle motion and for this reason we use this approach in § 3.1 to provide a physical understanding of the cross-stream driving forces.

3.1. *Physical origin of the cross-stream force on an asymmetric two-dimensional particle*

In this subsection we adopt a resistivity formulation and consider the forces per unit area acting on an axisymmetric ring-shaped particle that is held fixed in the x–z-plane and on a two-dimensional particle that constitutes the local cross-section of this ring-shaped particle. We will be particularly interested in the net torque that would tend to

https://doi.org/10.1017/jfm.2013.53 Published online by Cambridge University Press

drive the axisymmetric particles to rotate with or against the vorticity and the net force per unit area on the local cross-section that contributes to this torque.

The forces acting on a typical particle such as a spheroid held stationary in simple shear flow are shown in figure 1(*a*). The surface forces per unit area f_x in the x-direction create a fluid velocity disturbance that cancels the externally imposed simple shear flow at the particle surface. These x-forces also create a disturbance velocity in the y-direction which gives rise to a surface force in the y-direction on the surface of the particle to satisfy the no-slip boundary condition. The net torque due to the combination of these forces rotates the particle in the direction of vorticity. For a particle with fore–aft symmetry the net force acting is 0. But a particle without fore–aft symmetry in simple shear flow can have a cross-stream force acting on it due to the extensional component of the flow. We present one such shape (figure 1*c*) which, when force-free, can undergo drift in a direction perpendicular to the direction of flow.

Let us consider a ring (figure 1*d*) of perturbed circular cross-section. If the radius of the unperturbed circular cross-section is c and the radius of the perturbed cross-section is scaled with c, the shape of the perturbed cross-section is given by:

$$R(\beta) = 1 + \alpha \cos(3\beta), \tag{3.2}$$

where R is the radius of the perturbed cross-section as a function of β, α is again the asymmetry parameter, and β is the angular coordinate in the local polar coordinate system measured relative to the line connecting the centre of the ring to the centre of the cross-section. Note here that the coordinate β is differently defined from the β used by Bretherton in the local spherical coordinate system of his aligning particle shape. Let the radius of the ring non-dimensionalized with c be A, measured from the centre of the global coordinate system whose origin is at the centre of the ring to the centre of the cross-section as shown in figure 1(*d*). We define the aspect ratio of the ring as the ratio of the radius of the circular cross-section to the radius of the ring, i.e. $\kappa = 1/A$.

For $A \gg 1$, one can locally approximate the ring as a straight infinite cylinder. Thus, a small part of the ring of thickness $(A\,\mathrm{d}\theta)$ can be modelled as an infinitely long cylinder held at an angle θ to the simple shear flow (figure 3*a*), where θ is the azimuthal angle measured from the vorticity direction in the flow–vorticity plane. Using linear superposition of Stokes flow solutions, the flow over an infinitely long cylinder inclined at an angle (θ) can be divided into two parts: (i) flow parallel to a long cylinder (figure 3*b*) with a $\cos\theta$ component of the shear flow acting over it; and (ii) flow perpendicular to a long cylinder with a $\sin\theta$ component of the flow acting (figure 3*c*).

The problem is now reduced to the solution of the force acting on an infinite cylinder aligned with its axis in the flow direction as shown in figure 3(*b*) and an infinite cylinder aligned with its axis in the vorticity direction as shown in figure 3(*c*). The undisturbed flow fields for the two problems in the new coordinate systems are now given by:

$$v_{x^*} = 0, \quad v_y = 0, \quad v_{z^*} = -y\cos\theta, \tag{3.3}$$

$$v_{x^*} = y\sin\theta, \quad v_y = 0, \quad v_{z^*} = 0, \tag{3.4}$$

where all the length scales are non-dimensionalized using the radius (c) of the undeformed ring cross-section, and the velocity gradients are non-dimensionalized using the shear rate, γ, of the simple shear flow. In the following discussion stresses are non-dimensionalized with $\mu\gamma$. The above flows are simple shear flows with $\cos\theta$

https://doi.org/10.1017/jfm.2013.53 Published online by Cambridge University Press

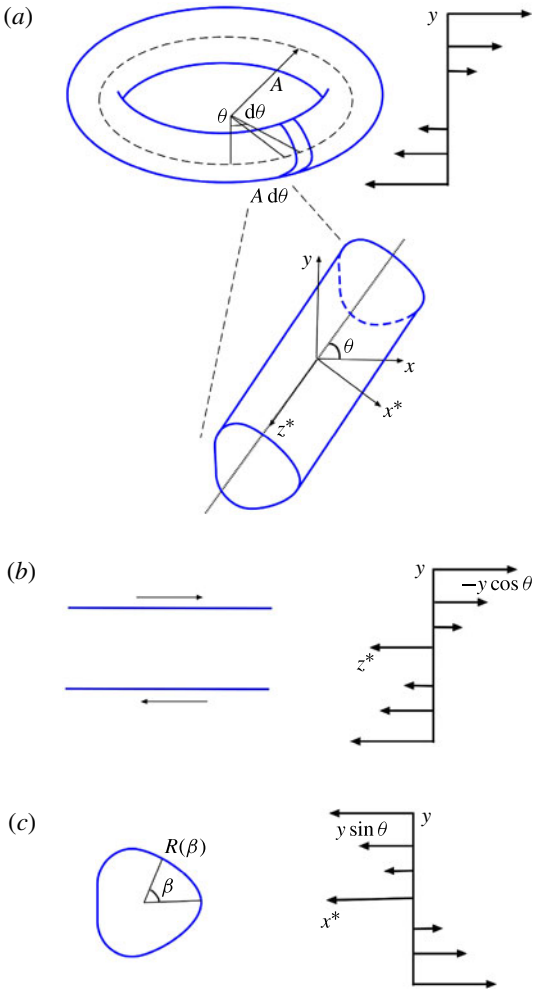


FIGURE 3. (Colour online) In the limit when $A \gg 1$, a small cross-section of a ring (*a*) inclined at an angle θ to the flow–gradient plane can be divided into two parts: an infinitely long cylinder aligned parallel (*b*) to the flow direction and an infinitely long cylinder perpendicular (*c*) to the flow–gradient plane.

and $\sin\theta$ as the new non-dimensionalized shear rates; z^* is the local coordinate along the axis of the ring and r is the local radial coordinate.

For case (i), in which the cylinder is aligned in the direction of flow, one can neglect the end effects of the cylinder on the disturbance field in the limit when the cylinder is infinitely long. This assumption implies that the flow is everywhere parallel to the axis of the cylinder, i.e. $v_{x^*}, v_y = 0$ with $v_{z^*}(r, \beta)$ the only non-zero component of the velocity. With flow parallel to the axis one can say that the pressure $p = 0$ since only variation in x^* and y are allowed and the velocity is perpendicular to these directions. The momentum balance equation then reduces to $\nabla^2 v_{z^*} = 0$. The flow applies a shear stress along the axis of the particle but no forces in the x^*–y-plane. There is no net force per unit length in the z^*-direction but rather a torque per unit length acting in the vorticity direction due to a force dipole as illustrated in figure 3(*b*).

https://doi.org/10.1017/jfm.2013.53 Published online by Cambridge University Press

In case (ii) (figure 3*c*), the imposed velocity in the x^*-direction induces stresses and a pressure variation in the x^*–y-plane and a net force per unit length in the y-direction. If we further decompose the shear in the x^*–y-plane into an extensional and a rotational component, we may note that the rotational fluid flow cannot induce a force. For a general three-dimensional particle, a fluid rotation far from the particle characterized by the vorticity $\boldsymbol{\omega}$ can induce a force

$$\boldsymbol{F} = \boldsymbol{H} \cdot \boldsymbol{\omega}, \tag{3.5}$$

where the resistance tensor $\boldsymbol{H}$ must be a pseudo-tensor. Since $\boldsymbol{H}$ depends only on the shape of the particle, this implies that the particle shape must be chiral. However, one cannot have a chiral two-dimensional particle so we conclude that the force due to fluid rotation in zero.

Thus, we will consider the fluid velocity and the force per unit length on the particle cross-section due to the extensional component of the shear flow. A complete treatment of this problem would require a slender-body theory with a quasi-two-dimensional inner solution matched to an outer solution in which the particle is treated as a ring of forces. The matching condition on the inner solution can be written in terms of the force per unit length F that the particle exerts on the fluid and a velocity of the fluid V relative to the ring produced by the deviation of the velocity disturbance of the ring of forces from that of an infinite line of forces as

$$v_r = \sin\theta \left[r \sin\beta \cos\beta + V \sin\beta + \frac{F}{2\pi}(\sin\beta - \sin\beta \ln r) \right], \tag{3.6a}$$

$$v_\beta = \sin\theta \left[\frac{r}{2}(\cos^2\beta - \sin^2\beta) + V \cos\beta - \frac{F\cos\beta}{2\pi} \ln r \right] \quad \text{as } r \to \infty. \tag{3.6b}$$

The no-slip boundary condition on the inner solution at the cylinder surface is

$$v_r = 0, \quad v_\beta = 0 \quad \text{at } r = R. \tag{3.7}$$

The inner solution is obtained by applying these boundary conditions to the general two-dimensional solution to Stokes equation written in terms of the stream function in a manner similar to that outlined for the mobility problem in § 3.2 below. In a full slender-body treatment, the relationship between V and F which depends on the particle aspect ratio would be obtained by matching the inner solution to an outer solution. However, for illustrative purposes we will examine the qualitative variation of the force on the particle surface for the inner solution in the case $V = 0$. In § 3.2, we will see that the quantitative cross-stream migration rate can be obtained from the inner solution in a mobility formulation without the need to match to an outer solution.

Before considering the forces acting on an infinitely long cylinder with the asymmetric cross-section given by (3.2), let us first consider a cylinder with circular cross-section. The forces on the surface of the cylinder in pure extensional flow are shown in figure 4(*a*). Due to the symmetry of the shape, the forces on the circle in opposite quadrants cancel each other. When the cross-sectional shape is not fore–aft symmetric, the forces on the particle in opposite quadrants no longer cancel each other. Figure 4(*b*) shows the forces acting on the rod when the shape of the cross-section is given by (3.2). The net force in the x^*-direction is still zero but there is a net force in the y-direction. This effect can be seen more clearly in figure 4(*c*) which represents the difference between the y-components of the forces on the asymmetric and the circular cross-sections.

https://doi.org/10.1017/jfm.2013.53 Published online by Cambridge University Press

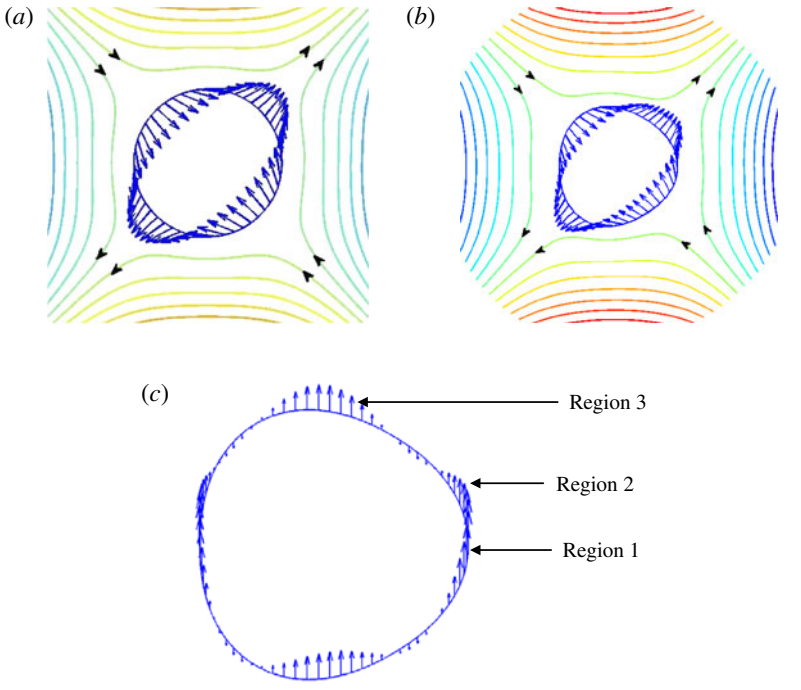


FIGURE 4. (Colour online) Comparison of forces on circular and non-circular cross-sections in extensional flow. (*a*) Forces acting on a long cylinder with circular cross-section in extensional flow. The surface of the cross-section and the forces are in blue colour; the other coloured lines indicate streamlines. (*b*) Forces acting on a long cylinder with non-circular cross-section $(1 + 0.1\cos 3\beta)$ in extensional flow. The surface of the cross-section and the forces are in blue; the other coloured lines indicate streamlines. (*c*) Difference of forces in the lateral direction between a circular and a non-circular cross-section cylinder. The three regions in a quadrant where net lateral forces are acting are shown here.

Now let us consider the physical mechanisms leading to a net positive y-component of the force on the asymmetric particle. In figure 4(*c*), we have highlighted three regions of the first quadrant of the particle where the asymmetry increases the force per unit area in the y-direction, f_y. We will explain the origin of the extra force in these regions; the mechanisms leading to extra f_y in the other quadrants are similar. We can write f_y in terms of the components of the stress tensor as:

$$f_y = \sigma_{yy} n_y + \sigma_{yx^*} n_{x^*}. \tag{3.8}$$

The primary contribution to the yy-stress, σ_{yy}, comes from the pressure, while the primary contribution to σ_{yx^*} is from the viscous stress; n_{x^*} and n_y are the components of the normal vector to the surface in the x^*- and y-directions. In region 1, the asymmetric particle extends radially outward further into the flow than the circle, increasing the velocity gradient and the viscous stress contribution to σ_{yx^*}. The lift force in region 2 arises primarily from the first term in (3.8). However, we found that the pressure and σ_{yy} do not change substantially. Instead it is the variation of the y-component of the unit normal with particle shape, given to $O(\alpha)$ by

$$n_y = \cos\beta + 3\alpha\cos\beta\sin 3\beta, \tag{3.9}$$

https://doi.org/10.1017/jfm.2013.53 Published online by Cambridge University Press

that accounts for the increased pressure-induced y-force. Similarly, in region 3, an increase in n_{x^*} leads to a larger viscous stress contribution to the y-force. This can be seen by noting that n_{x^*} is given by

$$n_{x^*} = \cos\beta - 3\alpha \sin\beta \sin 3\beta \tag{3.10}$$

and region 3 corresponds to $\beta > \pi/3$ and $\sin 3\beta < 0$ as well as being a region with a high shear stress.

3.2. *Derivation of the cross-stream velocity*

In this subsection, we will perform a detailed asymptotic analysis to determine the drift velocity of an asymmetric two-dimensional particle and the resulting rotation rate of a ring with an asymmetric cross-section. Particles are known to migrate across streamlines in unidirectional flows due to asymmetry (Brenner 1964; Nir & Acrivos 1973), deformability (Goldsmith & Mason 1962; Olla 1999), inertia (Ho & Leal 1974; Vasseur & Cox 1976), and non-Newtonian behaviour of the fluid (Ho & Leal 1976). The migration of the particle due to inertia, deformability and the non-Newtonian behaviour of the fluid requires a combination of linear and quadratic flow or particle–wall hydrodynamic interactions in a bounded simple shear flow. However, an asymmetric particle can migrate in an unbounded simple shear flow. This migration is dependent on the orientation of the particle relative to the shear flow. Nir & Acrivos (1973) considered a freely suspended asymmetric particle and found that it underwent a time-periodic cross-stream migration with no net migration averaged over the particle period of rotation. Brenner (1964) considered a resistivity problem for an asymmetric particle and showed that either rotation of the particle or an imposed extensional flow can cause a cross-stream force. In our case, the two-dimensional particle is the cross-section of a ring and the connectedness of the ring can prevent its rotation. To determine the rotation rate in a mobility formulation for the entire ring when the ring is aligned in the x–z-plane, we will be interested in the cross-stream y-velocity on a two-dimensional particle aligned in the x^*-direction. If the stresses created by the component of shear flow perpendicular to the local axis of the ring (3.4) lead to a particle rotation rate (torque) that exceeds that created by the component of the shear flow parallel to the local axis (3.3), the particle will tend to rotate against the vorticity when it is in the x–z-plane and will achieve a fixed orientation upstream of the x–z-plane.

Here, we first calculate the drift velocity of a particle lacking fore–aft symmetry across streamlines in two-dimensional flow. We find that the drift velocity of the two-dimensional fore–aft-asymmetric cross-section is distributed over the ring such that it creates a rigid-body rotation in a direction opposite to the vorticity direction. This rigid-body rotation, in the asymptotic limits of $A \gg 1$ and $\alpha \ll 1$, allows us to simply superimpose the angular velocity due to the fore–aft symmetry on the Jeffery-type angular velocity of the ring in simple shear. In the next subsection, we use the balance between the two angular velocities to obtain the condition for alignment of the particle.

The shape of the cross-section is represented using Fourier modes with the coefficient of the mode (α) being small. We derive the leading-order drift velocity of the cross-section by expanding in a regular perturbation expansion in α. To keep the discussion general, let the shape of the cross-section be given by:

$$R(\beta) = 1 + \alpha \cos((2m+1)\beta) \quad \text{for } m \geqslant 1, \tag{3.11}$$

https://doi.org/10.1017/jfm.2013.53 Published online by Cambridge University Press

where α is a small parameter. Only odd Fourier modes are considered here as even modes are fore–aft symmetric and cannot lead to a cross-stream drift. We solve for the drift velocity of a force-free non-rotating particle in the undisturbed flow field given by (3.4).

Let the unknown drift velocity of the particle be v_1 in $+y$-direction. We use the stream function approach to solve the Stokes flow problem in two dimensions. The general solution for the stream function (Leal 2007) is used along with the boundary conditions that, far from the particle, the fluid velocity is given by simple shear and, on the surface of the particle, the fluid velocity is equal to v_1 in $+y$-direction. Writing the undisturbed velocity field at $r \to \infty$ in polar coordinates:

$$v_r = r\sin\theta\sin\beta\cos\beta, \quad v_\beta = -r\sin\theta\sin^2\beta. \tag{3.12}$$

In polar coordinates, the velocity field is related to the stream function as:

$$v_r = \frac{1}{r}\frac{\mathrm{d}\psi}{\mathrm{d}\beta}, \quad v_\beta = -\frac{\mathrm{d}\psi}{\mathrm{d}r} \tag{3.13}$$

so the boundary condition (3.13) expressed in terms of the stream function is:

$$\psi|_{r\to\infty} = \sin\theta\frac{r^2(1-\cos(2\beta))}{4} + c_1. \tag{3.14}$$

Using the general solution (Leal 2007) for the stream function in polar coordinates, the stream function may be expressed as:

$$\begin{aligned}\psi = {} & \sin\theta\frac{r^2(1-\cos(2\beta))}{4} + c_1 + c_2\ln(r) + d_1\frac{\cos(\beta)}{r} + d_2\frac{\cos(2\beta)}{r^2} + \hat{d}_2\frac{\cos(2\beta)}{r^0} \\ & + d_3\frac{\cos(3\beta)}{r^3} + \hat{d}_3\frac{\cos(3\beta)}{r^1} + d_4\frac{\cos(4\beta)}{r^4} + \hat{d}_4\frac{\cos(4\beta)}{r^2} \\ & + d_5\frac{\cos(5\beta)}{r^5} + \hat{d}_5\frac{\cos(5\beta)}{r^3} + \cdots d_n\frac{\cos(n\beta)}{r^n} + \hat{d}_n\frac{\cos(n\beta)}{r^{n-2}} + \cdots .\end{aligned} \tag{3.15}$$

Here we have included only those terms in the stream function corresponding to the imposed simple shear flow equation (3.14) and a velocity disturbance due to the particle that is required to decay as $r \to \infty$. In addition we have omitted terms that involve sine functions owing to the symmetry of the particle and flow about the x^*–z^*-plane.

To find the unknown constants in (3.15), the no-slip boundary condition at the surface of the particle is used:

$$v_r = v_1\sin(\beta) = \frac{1}{r}\frac{\mathrm{d}\psi}{\mathrm{d}\beta}, \tag{3.16a}$$

$$v_\beta = v_1\cos(\beta) = -\frac{\mathrm{d}\psi}{\mathrm{d}r} \quad \text{at } r = 1 + \alpha\cos((2m+1)\beta). \tag{3.16b}$$

Using (3.15), these conditions can be written as:

$$\begin{aligned}v_1\sin(\beta)|_{r=R} = {} & \frac{\sin\theta}{2}R\sin(2\beta) + 0 - \frac{d_1\sin(\beta)}{R^2} - \frac{2d_2\sin(2\beta)}{R^3} \\ & - \frac{2\hat{d}_2\sin(2\beta)}{R} + \cdots - \frac{nd_n\sin(n\beta)}{R^{n+1}} - \frac{n\hat{d}_n\sin(n\beta)}{R^{n-1}} + \cdots ,\end{aligned} \tag{3.17}$$

https://doi.org/10.1017/jfm.2013.53 Published online by Cambridge University Press

$$v_1\cos(\beta)|_{r=R} = -\frac{\sin\theta}{2}R(1-\cos(2\beta)) - \frac{c_2}{R} + \frac{d_1\cos(\beta)}{R^2}\frac{2d_2\cos(2\beta)}{R^3} + 0 + \cdots + \frac{nd_n\cos n\beta}{R^{n+1}} + \frac{(n-2)\hat{d}_n\cos n\beta}{R^{n-1}} + \cdots. \tag{3.18}$$

Using the above boundary conditions on the surface of the particle, we calculate the drift velocity v_1 as well as the unknown coefficients c_2, d_1, d_2, $\hat{d}_2\ldots$ used to describe the stream function in (3.15). The process involves expressing terms in (3.17) and (3.18) in terms of sine and cosine Fourier modes respectively and using orthogonality of Fourier series to solve for the unknown coefficients.

First, we consider a circular cylinder so that $\alpha = 0$ and $R = 1$. Using the surface boundary conditions (3.16) with $\alpha = 0$, we get (Bretherton 1962*b*):

$$\psi = \sin\theta\left[\frac{r^2(1-\cos(2\beta))}{4} - \frac{\ln(r)}{2} - \frac{\cos(2\beta)}{4r^2} + \frac{\cos(2\beta)}{2r^0}\right]. \tag{3.19}$$

The only non-zero Fourier mode is the second mode driven by the $\cos(2\beta)$ term of the simple shear flow stream function when the surface of the particle is circular. In this case, there is no drift velocity, i.e. $v_1 = 0$. The solution for the stream function around an infinitely long circular cylinder rotating in a simple shear flow was first given by Bretherton (1962*b*); the above relation (3.19) is a special case of that solution when angular velocity of the cylinder is 0.

Next we consider the first perturbation to the stream function due to finite asymmetry. When $\alpha \neq 0$, the $O(\alpha^0)$ terms in the solution for the stream function in the presence of a circle are the terms that drive other modes of the stream function at $O(\alpha)$. In particular the perturbed flow is driven by the interaction of the $(2m+1)$ mode of the perturbed surface and the $O(1)$ $\cos(2\beta)$ terms and the $\ln(r)$ term in (3.19). To the leading order any term in (3.17) and (3.18) can be written as:

$$R^a\sin 2\beta = (1 + a\alpha\cos((2m+1)\beta))\sin 2\beta = \sin 2\beta + a\alpha(\sin((2m+3)\beta) - \sin((2m-1)\beta)), \tag{3.20a}$$

$$R^a = 1 + a\alpha\cos((2m+1)\beta), \tag{3.20b}$$

$$R^a\cos 2\beta = \cos 2\beta + a\alpha(\cos((2m+3)\beta) + \cos((2m-1)\beta)), \tag{3.20c}$$

where (3.20*a*) gives the type of term needed in (3.17) and (3.20*b*) and (3.20*c*) the types of terms needed in (3.18). It should be noted here that in both (3.17) and (3.18), the same Fourier modes appear, except that in one case all terms are expressed in terms of sine functions and in the other in terms of cosine functions. The other difference is the $1/r$ (from $\ln r$) term which appears only in (3.18) and drives the $2m+1$ mode. Thus, to the leading order it turns out that only $2m-1$, $2m+1$ and $2m+3$ Fourier modes terms are non-zero in the general stream function solution (3.15). All other modes are higher-order in α.

Since we are interested in shapes for which $v_1 \neq 0$, it is valuable to note that the only term that can drive the v_1 term to first-order is the first Fourier mode, which is non-zero for $m = 1$. Hence, amongst the family of shapes represented by (3.11), the only shape with a non-zero drift velocity is that with the third Fourier mode (3.2)

https://doi.org/10.1017/jfm.2013.53 Published online by Cambridge University Press

perturbation. The solution of the stream function for such a shape is given by:

$$\psi = \sin\theta \left[\frac{r^2(1-\cos(2\beta))}{4} - \frac{\ln(r)}{2} - \frac{\cos(2\beta)}{4r^2} - \frac{\alpha\cos(\beta)}{2r} + \frac{\cos(2\beta)}{2r^0} + \frac{\alpha\cos(3\beta)}{2r^3} - \frac{\alpha\cos(3\beta)}{2r^1} - \frac{\alpha\cos(5\beta)}{2r^5} + \frac{\alpha\cos(5\beta)}{2r^3} \right], \tag{3.21}$$

and the drift velocity in this case is:

$$v_1 = \frac{\alpha\sin\theta}{2}. \tag{3.22}$$

3.3. *Condition for alignment*

The drift velocity, v_1, to the leading order is proportional to α, a measure of the degree of asymmetry of the cross-section. When this cross-section becomes part of the ring, one can calculate an angular velocity originating from this drift velocity. The $\sin\theta$ dependence of the drift velocity for a cross-section corresponds to a solid-body rotation of the ring. The corresponding rigid-body rotation rate of the ring in the vorticity direction when its axis of symmetry is in the gradient direction is given by:

$$-\omega_{as} A \sin\theta = v_1, \tag{3.23a}$$

$$\omega_{as} = -\frac{\alpha}{2A}. \tag{3.23b}$$

The angular velocity of the ring in (3.23) arises from the asymmetry of the cross-section and is opposite to the direction of vorticity. Apart from this angular velocity, a finite-aspect-ratio ring will undergo rotation in the vorticity direction due to the torque per unit length exerted by the shear flow. In the limit when $\alpha \ll 1$, the leading-order angular velocity of the ring is the same as the angular velocity of a ring with circular cross-section in simple shear flow. The torque per unit length arises from a local interaction of the flow with the ring cross-section and is independent of A, and this leads to a total torque proportional to the circumference $2\pi A$. The resistance to rotation is proportional to $\ln A/A^3$ so the rotation rate induced by the torque is proportional to $(\ln A)/A^2$. Thus the angular velocity in the vorticity direction is given by:

$$\omega_{cc} = 0.815\frac{\ln A}{A^2} + O\left(\alpha\frac{\ln A}{A^2}\right) \tag{3.24}$$

where the prefactor of the leading-order term in (3.24) was obtained using the boundary-element method simulations presented in § 5.

The net angular velocity of a ring in the vorticity direction, in the limits $A \gg 1$ and $\alpha \ll 1$, can be calculated using linear superposition of angular velocities calculated in (3.23) and (3.24), and is then given by:

$$\omega = \frac{1+\lambda}{2} = 0.815\frac{\ln A}{A^2} - \frac{\alpha}{2A} + O\left(\alpha\frac{\ln A}{A^2}\right). \tag{3.25}$$

Here, the tumbling parameter, λ, is written in terms of the angular velocity of the particle using (1.1) and the knowledge that the particle is oriented in the gradient direction. It should be noted here that there are two $O(\alpha)$ terms in (3.25); however the $O(\alpha(\ln A/A^2))$ term can be neglected compared to $\alpha/2A$ when $A \gg 1$.

https://doi.org/10.1017/jfm.2013.53 Published online by Cambridge University Press

The particle will reach a steady alignment if the tumbling parameter is less than or equal to -1. This occurs when the rotation rate of a particle in the flow–gradient plane is less than or equal to zero, which corresponds to the angular velocity due to the asymmetry of the particle being greater than or equal to the angular velocity of the particle with the circular cross-section. This condition is given by:

$$\frac{\alpha}{2A} \geqslant 0.815\frac{\ln A}{A^2}, \tag{3.26a}$$

$$\alpha \geqslant 1.63\frac{\ln A}{A}. \tag{3.26b}$$

The 'equal to' sign in the above equation corresponds to a critical radius of the ring at which the particle first aligns and has a permanent orientation within the flow–vorticity plane. A radius above this critical value leads to alignment of the axis of symmetry of the particle as noted earlier, at an angle ϕ to the gradient direction given by $\tan\phi = -((\lambda+1)/(\lambda-1))^{1/2}$. It should be noted here that unlike Bretherton's (Bretherton 1962*a*) shape, the ring shape presented here can align at a moderate aspect ratio. A challenge to achieve alignment with Bretherton's shape is the need for the asymmetric beads to overcome the torque on the connecting rod. In our shape there is no need for a connector and the entire circumference of the ring is providing a cross-stream force that contributes to the torque that is opposite to the vorticity direction. Another distinction is that the non-tumbling shapes studied in this work have $\lambda \leqslant -1$ whereas for Bretherton's shape $\lambda \geqslant 1$. Both our particle shape and Bretherton's are able to achieve alignment without an external body force or torque.

Thus far, we have described the cross-stream migration of a two-dimensional circular particle perturbed by the third Fourier mode and its role in creating a flow-aligning ring-shaped particle. We now discuss other perturbed shapes. Based on tensor symmetries discussed at the beginning of § 3, it is clear that fore–aft asymmetry is required to create cross-stream migration. However, it is interesting to note that not all fore–aft asymmetries could give rise to a lateral migration. It will be shown in § A.1 that any perturbed shape of the form

$$R = 1 + \alpha\cos((2m+1)\beta) \quad \text{for } m > 1, \tag{3.27}$$

corresponding to modes higher than third-order gives no migration velocity to any order in α. Thus, a ring with the cross-sectional shapes represented by (3.27) can align in simple shear flow only for $m = 1$.

Although shapes represented by (3.27) do not drift in the gradient direction, we find that combinations of perturbations involving higher-order modes could give rise to a lateral force at higher-orders in α. For example, a combination of Fourier modes of the form

$$R = 1 + \alpha_1\cos((2m_1+1)\beta) + \alpha_2\cos((2m_2+1)\beta) \tag{3.28}$$

can give a drift velocity for $m_1 = 2$ and $m_2 = 3$ as shown in § A.1.

4. Boundary-element method

The asymptotic solutions obtained above are valid only in the limits $A \gg 1$ and $\alpha \ll 1$; at finite A and α the problem needs to be solved using a numerical scheme. Both the resistivity and mobility problems discussed are ideally suited to be solved using the boundary-element method (Youngren & Acrivos 1975; Kim & Karilla 1991; Pozrikidis 2002), which solves an integral representation of the creeping-flow problem

https://doi.org/10.1017/jfm.2013.53 Published online by Cambridge University Press

on the two-dimensional surface of the particle instead of solving the Stokes equations in the three-dimensional domain. The starting point for the boundary-element method is an integral equation for the velocity field written in terms of the stresses acting on the boundary convoluted with the Green's function. The general integral representation of the creeping-flow problem was obtained by Ladyzhenskaya (1963). For the case of flow around rigid boundaries, the simplified integral equation (Kim & Karilla 1991) for the creeping-flow problem can be written as:

$$\boldsymbol{v}(\boldsymbol{r}) = \boldsymbol{u}(\boldsymbol{r}) + \int_S \boldsymbol{J}(\boldsymbol{r} - \boldsymbol{r}') \cdot \boldsymbol{f}(\boldsymbol{r}')\, \mathrm{d}S', \tag{4.1}$$

where $\boldsymbol{r}$ and $\boldsymbol{r}'$ are position vectors, $\boldsymbol{v}$ is the velocity on the boundary, $\boldsymbol{u}$ is the undisturbed fluid velocity (simple shear flow here) in the absence of the boundary, $\boldsymbol{f}$ is the unknown stress, S represents the boundary of the flow domain, $\mathrm{d}S'$ indicates integration over S with respect to the point $\boldsymbol{r}'$, and $\boldsymbol{J}$ is the Green's function. The integral term on the right-hand side represents the disturbance field created by the stresses at $\boldsymbol{r}'$ on the velocity at $\boldsymbol{r}$. For the Stokes problem, $\boldsymbol{J}$ is given by:

$$J_{ij} = \frac{1}{8\pi}\left(\frac{\delta_{ij}}{r} + \frac{r_i r_j}{r^3}\right). \tag{4.2}$$

Based on the symmetry of the particle studied here about the x–z-plane and the antisymmetry of the flow about the x–z-plane, we can further simplify the problem by identifying the following relationship between stresses acting on the surface of the particle:

$$f_x(\boldsymbol{\rho}, +y) = -f_x(\boldsymbol{\rho}, -y), \quad f_y(\boldsymbol{\rho}, +y) = f_y(\boldsymbol{\rho}, -y), \quad f_z(\boldsymbol{\rho}, +y) = -f_z(\boldsymbol{\rho}, -y), \tag{4.3}$$

where $\boldsymbol{\rho}$ is the radial vector in polar coordinates in the x–z-plane. Using the above relations, the boundary integral formulation for the problem is then reduced to:

$$\begin{aligned} v_i(\boldsymbol{r}) - \Gamma_{ij} r_j = \int_S \mathrm{d}S' (&f_y(\boldsymbol{\rho}', y')[J_{iy}(\boldsymbol{\rho} - \boldsymbol{\rho}' + \boldsymbol{e}_y(y - y')) + J_{iy}(\boldsymbol{\rho} - \boldsymbol{\rho}' + \boldsymbol{e}_y(y + y'))] \\ &+ f_x(\boldsymbol{\rho}', y')[J_{ix}(\boldsymbol{\rho} - \boldsymbol{\rho}' + \boldsymbol{e}_y(y - y')) - J_{ix}(\boldsymbol{\rho} - \boldsymbol{\rho}' + \boldsymbol{e}_y(y + y'))] \\ &+ f_z(\boldsymbol{\rho}', y')[J_{iz}(\boldsymbol{\rho} - \boldsymbol{\rho}' + \boldsymbol{e}_y(y - y')) - J_{iz}(\boldsymbol{\rho} - \boldsymbol{\rho}' + \boldsymbol{e}_y(y + y'))]), \end{aligned} \tag{4.4}$$

where $\boldsymbol{\Gamma}$ is the non-dimensional imposed velocity gradient tensor. The integration is now performed on the surface of the particle in the $+y$-direction.

Given the axisymmetry of the particle, the unidirectional nature of the imposed flow and the orientation of the particle with respect to the external flow, one can expect a simple dependence of stresses on the θ-direction. Using the finite-element software package Comsol, we have determined the following functional dependence of the stresses on the azimuthal (θ) direction:

$$f_x(\boldsymbol{\rho}, +y) = f_1(\rho, +y)\cos(2\theta) + f_2(\rho, +y), \tag{4.5a}$$

$$f_y(\boldsymbol{\rho}, +y) = f_3(\rho, +y)\cos\theta, \tag{4.5b}$$

$$f_z(\boldsymbol{\rho}, +y) = f_4(\rho, +y)\sin(2\theta). \tag{4.5c}$$

These finite-element Comsol simulations have been performed in a manner similar to the ones described in Singh, Koch & Stroock (2011) for determining effective aspect ratio of cylindrical disks. Using the above dependence of stresses on the azimuthal direction in (4.4), we analytically integrate along the azimuthal direction. These results are shown in § A.2. The remaining problem is then reduced to numerical integration

https://doi.org/10.1017/jfm.2013.53 Published online by Cambridge University Press

along the radial direction and requires discretization only over the cross-section of the ring. It should be noted here that in the limit $\boldsymbol{\rho} \to \boldsymbol{\rho}'$, the Green's functions in (4.4) are singular. Analytical integration is performed to remove the singularities in this limit. The details of the analytical integration are also given in § A.2.

For the simulations, the ring cross-section is discretized into N elements. Each element subtends an equal angle $\mathrm{d}\beta$ at the centre of the ring cross-section and the entire cross-section is at a constant value of θ from the vorticity direction. The stresses over the individual elements are considered to be constant. Each element itself is locally divided into N_{small} elements to integrate the Green's function. For the results presented in this work, we have taken $N = 500$ and $N_{small} = 20$.

In the present work, we solve two types of problem: (i) determine the angular velocity of a torque-free particle (mobility problem); and (ii) determine the torque acting on a stationary particle (resistivity problem). For solving the resistivity problem (type ii), the surface velocity of 0 is used in the integral equation and the problem is solved for the stresses (f_1, f_2, f_3, f_4) acting on the particle which corresponds to $4N$ variables. Momentum balances in three directions yield $3N$ linear equations for N elements for a single constant value of θ. An additional N equations are obtained by applying the momentum balance in the x-direction (A 5) for another value of θ. The two constant values of θ used in the simulations are: $\pi/4$ for momentum balances in all three directions and 0 for momentum balance in the x-direction. The resultant torque is calculated from the stresses using the following equation:

$$\begin{aligned} T_z &= 2\int_S \mathrm{d}S(yf_x - \rho\cos\theta f_y) \\ &= 2\int_S \mathrm{d}S(y(f_1\cos 2\theta + f_2) - \rho\cos^2\theta f_3). \end{aligned} \tag{4.6}$$

The factor of 2 in the above equation accounts for the torque acting on the $-y$ half of the particle which by symmetry of the flow about x–z-plane and fore–aft symmetry of the particle is equal in magnitude and direction to the torque acting in the $+y$ half of the particle.

For the solution of the mobility problem (type i), an unknown angular velocity, ω, along the vorticity direction is assumed. The velocity boundary conditions on the surface of the particle for this case are then given by:

$$v_x = \omega y, \tag{4.7a}$$

$$v_y = -\omega\rho\cos\theta. \tag{4.7b}$$

In the simulations for this case, there are $4N + 1$ unknowns, with angular velocity ω of the ring being an additional unknown. The condition of no net torque, $T_z = 0$, is applied to (4.6) to solve for the additional unknown.

5. Numerical and analytical predictions

In this section we present the results of the boundary-element simulations and compare these results with the analytical predictions derived in § 3. We first validate our implementation of the boundary-element method (BEM) by comparing with analytical predictions for the torque on a circular ring rotating in a quiescent fluid. The analytical results are then compared with the simulation results in the limit when $\alpha \ll 1$ and $A \gg 1$. Finally, BEM results for finite aspect ratios and finite α values for the ring particles with cross-section given by (3.2) are presented. We determine the critical α-dependent radius of the ring, A, at which the ring will transition from

https://doi.org/10.1017/jfm.2013.53 Published online by Cambridge University Press

rotating continuously to reaching a steady alignment. The resistance formulation is used for the validation of the torque results in § 5.1, while all the other results involve calculation of the angular velocity for a freely rotating ring using the mobility formulation.

5.1. *Circular cross-section ring*

When $\alpha = 0$, the particle cross-section is circular and the ring has the shape of a circular torus. The torque and the rotation rate of such a ring with its axis of symmetry in the gradient direction of a simple shear flow satisfy the relationship:

$$T_z - 8\pi g_z (A+1)^3 \left(\omega - \frac{1+\lambda}{2}\right) = 0. \tag{5.1}$$

Here, two parameters, the tumbling parameter λ and the torque coefficient g_z, allow one to calculate the torque on a particle rotating with any angular velocity ω in simple shear flow. We calculated the tumbling parameter λ of the particle by solving for the angular velocity of the particle when the particle is torque-free ($T_z = 0$) from the BEM simulations of the mobility problem. The torque coefficient is then calculated based on the BEM simulations of the resistivity problem ($\omega = 0$). Our results for the torque coefficient can be compared with previous theoretical work while we obtain new predictions for the tumbling parameter of a circular torus.

Circular-torus-shaped particles have been extensively studied in the past (Tchen 1954; Pell & Payne 1960; Yamakawa & Yamaei 1973; Johnson & Wu 1979; Goren & O'Neill 1980; Thaokar, Schiessel & Kulic 2007) particularly because of interest in ring polymers. We will compare our simulation results with the complete solutions of Goren & O'Neill (1980) and the asymptotic solutions of Johnson & Wu (1979). Goren & O'Neill (1980) have determined the torque and force on rotating and translating circular-torus particles in a fluid that is at rest at infinity. They obtained analytical results even for finite-aspect-ratio particles by solving the equations of motion for the fluid in toroidal coordinates. In particular, we will consider their analytical results for the torque coefficient calculated for a torus rotating about one of its long axes.

The scaling of the torque coefficient at high aspect ratio is obtained from the results of Johnson & Wu (1979) who used the singularity solution for Stokes flow to solve for the flow past a slender ring with circular cross-section. Johnson & Wu calculated the force per unit length and the torque per unit length acting on the ring cross-section; we present two leading terms for the torque coefficient of the particle at large A which are generated by the force per unit length term. In the limit $A \gg 1$, the force per unit length is given by $(= -8\pi(((1+\lambda)/2)A/2(\ln 8A - 3/2))\sin\theta + O(1/A^2))$ for rings rotating about one of their longer axes where θ is the angle relative to the axis of rotation. The torque acting on the particle due to this force can then be written as:

$$\begin{aligned} T_z &= \int_0^{2\pi} 8\pi \left(\frac{((1+\lambda)/2)A}{2\left(\ln 8A - \frac{3}{2}\right)}\right) \sin^2\theta A^2 \,\mathrm{d}\theta \\ &= 8\pi^2 \left(\frac{((1+\lambda)/2)A^3}{2\left(\ln 8A - \frac{3}{2}\right)}\right). \end{aligned} \tag{5.2}$$

Using (5.1) and (5.2), the torque coefficient is given by:

$$g_z = \frac{\pi}{(2\ln 8A - 3)}\left(1 - \frac{3}{A}\right) + O\left(\frac{1}{A^2}\right). \tag{5.3}$$

https://doi.org/10.1017/jfm.2013.53 Published online by Cambridge University Press

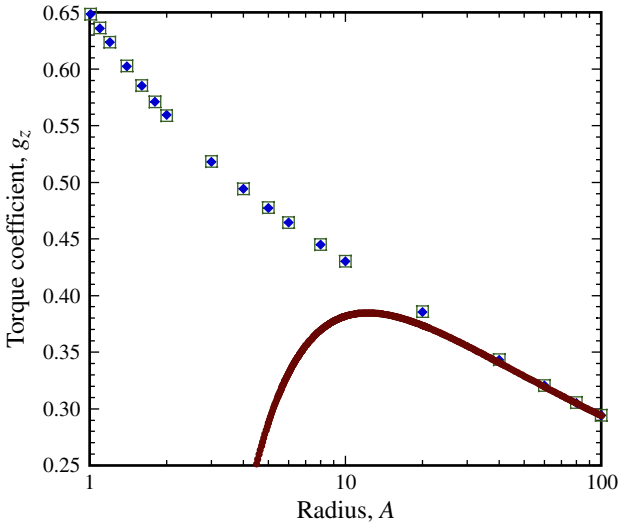


FIGURE 5. (Colour online) Comparison of torque coefficient, g_z, between complete analytical results (Goren & O'Neill 1980) (◇), BEM simulations (□), and asymptotic analysis (continuous curve, (5.3)) (Johnson & Wu 1979) for a circular cross-section ring ($\alpha = 0$).

Figure 5 presents a comparison of the complete analytical solution of torque coefficients obtained from table 1 of Goren & O'Neill (1980), torque coefficients obtained from Johnson & Wu (1979) using (5.3) and results from the BEM simulations. Our numerical predictions (□) are in very good agreement with the analytical predictions (◇) of Goren & O'Neill (1980) at all values of the ring radius. Johnson & Wu (1979)'s predictions (continuous curve) at small aspect ratio are in good agreement with the exact results when the non-dimensional radius of the ring is larger than 20.

The angular velocity ω_{cc} of a torque-free circular torus in the x–z-plane of a simple shear flow is plotted in figure 6 for A ranging from 1.5 to 250. The scaling analysis outlined in (3.24) indicating that the rotation rate is proportional to $\ln(A)/A^2$ is quantitatively accurate at small aspect ratios and remains a good approximation for A as small as 3. The tumbling parameter can be calculated from ω_{cc} using (5.1). The effective aspect ratio of the ring-shaped particle to the leading order is then given by:

$$\kappa_e = \left(\frac{1+\lambda}{2}\right)^{1/2} = \left(\frac{0.815\ln A}{A^2}\right)^{1/2} = 0.903\kappa\,(\ln(1/\kappa))^{1/2}\,. \tag{5.4}$$

It is interesting to note that slender circular rings like long cylindrical fibres rotate logarithmically faster than spheroids of the same aspect ratio (Cox 1971) (Note that Singh *et al.* 2011 incorrectly listed Cox's asymptotic effective aspect ratio of cylinders for $\kappa \gg 1$ as $1.24\kappa/\ln(\kappa)$ rather than $1.24\kappa/(\ln(\kappa))^{1/2}$ in their equation (9). However, the correct formula was used in figure 5 of Singh *et al.* 2011). In contrast, the effective aspect ratio of low-aspect-ratio circular disks (Singh *et al.* 2013) is larger than the particle aspect ratio by an algebraic factor.

5.2. *Comparison of asymptotic analysis with simulation for large A and small α*

Here, we compare our predictions from the asymptotic analysis of a thin ring in the limit when $A \gg 1$ and $\alpha \ll 1$ with the BEM simulations. A ring with a circular

https://doi.org/10.1017/jfm.2013.53 Published online by Cambridge University Press

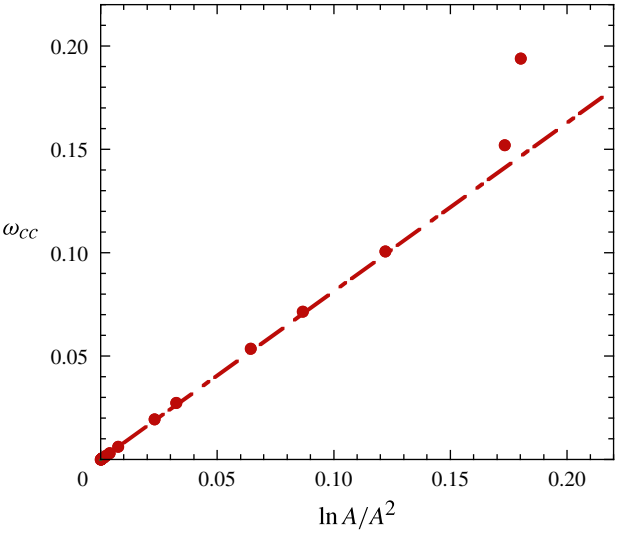


FIGURE 6. (Colour online) Angular velocity of a ring with circular cross-section for $A \geqslant 1.5$. The straight line fit is plotted using data for $A \geqslant 100$ and is given by $\omega_{cc} = 0.815(\ln A/A^2)$.

cross-section undergoes Jeffery's rotational motion in the vorticity direction in simple shear flow with an angular velocity, ω_{cc} (3.24). When the shape of the cross-section is slightly non-circular as given by (3.2), the angular velocity of the particle is a combination of this Jeffery's rotational velocity and an angular velocity due to the asymmetry of the cross-section of the ring. From the asymptotic analysis in § 3, we have shown that in the limit when $\alpha \ll 1$ and $A \gg 1$, the angular velocity, ω_{as} of the particle due to the asymmetric cross-section is given by (3.23). As noted earlier, the net angular velocity, ω, is given by:

$$2\omega = 1 + \lambda = 1.63\frac{\ln A}{A^2} - \frac{\alpha}{A} + O\left(\alpha\frac{\ln A}{A^2}\right). \tag{5.5}$$

It should be noted here that the angular velocity, ω_{cc}, also changes due to the change in the cross-section but is a factor of A^{-1} smaller than ω_{as} and can be neglected in the leading-order analysis. Figure 7 shows twice the angular velocity of the particle as a function of α for $A = 50$, 100 and 200. The straight lines are fits to the simulations for values of $\alpha < 0.02$. The slopes of these lines for $A = 200$ and 100 are found to be within 1.5 % of the predicted slope of $1/A$ from the analysis in (5.5). The slope of the line for $A = 50$ is ∼3 % less than the predicted slope. The intercept of the lines on the y-axis corresponds to twice the angular velocity of the particle with circular cross-section. The linear dependence of the rotation rate on α provides a good approximation to the computational results up to $\alpha \approx 0.08$. At higher α, the rotation rate decreases more slowly with α suggesting that backward rotation of the ring due to the asymmetry saturates at finite α.

5.3. *Finite-aspect-ratio calculations*

As the non-dimensional radius, A, of the ring becomes smaller and the deviation of the cross-section from a circular shape becomes more significant, the asymptotic approximations used in § 3 are no longer accurate. To explore the rotation rate of particles in this regime we perform a series of boundary-element simulations for a

https://doi.org/10.1017/jfm.2013.53 Published online by Cambridge University Press

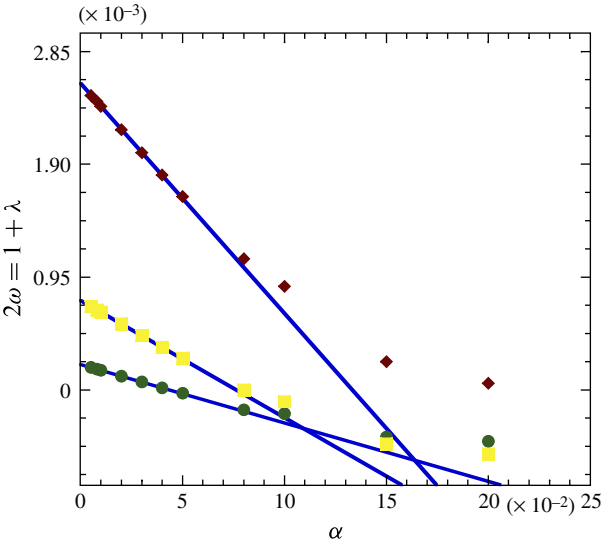


FIGURE 7. (Colour online) Angular velocity of the ring-shaped particles with axis of symmetry oriented in the gradient direction as a function of α for: $\diamond$, $A = 50$; $\square$, $A = 100$; and $\bigcirc$, $A = 200$; in the limit of small α. Equations of the lines for the three cases are: $2\omega = 2.58 \times 10^{-3} - 1.94 \times 10^{-2}\alpha$ for $A = 50$, $2\omega = 7.51 \times 10^{-4} - 9.86 \times 10^{-3}\alpha$ for $A = 100$, and $2\omega = 2.14 \times 10^{-4} - 4.93 \times 10^{-3}\alpha$ for $A = 200$.

range of A and α. Using (5.5), the tumbling parameter is calculated by solving for the torque-free angular velocity of the ring in the BEM. For practical purposes it is of interest to find the minimum radius (maximum aspect ratio) of the particle at which it will reach a steady alignment. Since the transition from tumbling to aligning motion occurs when the tumbling parameter λ is equal to -1, we plot $1 + \lambda$ as a function of the radius of the ring, A, for $\alpha = 0$, 0.1, 0.4 and 0.55 in figure 8. As A increases, $1 + \lambda$ decreases and crosses 0 which is the point of transition from tumbling to non tumbling. For the particles that stop rotating, the value of $1 + \lambda$ after reaching a minimum starts increasing with increasing A although it does not cross 0 again. This behaviour is consistent with the asymptotic analysis (5.5) which indicates that $1 + \lambda$ scales like $O(\alpha/A)$ for $A \gg 1$ and $\alpha \ll 1$.

For $\lambda + 1 < 0$, a particle axis of symmetry reaches a fixed orientation in the x–y-plane. The angle between the particle axis of symmetry and the gradient direction is given by $-\tan^{-1}((\lambda + 1)/(\lambda - 1))^{1/2}$ (figure 2) which, for $\lambda \sim -1$, can be simplified to just $-((1 + \lambda)/(-2))^{1/2}$. The maximum absolute value of the angle of inclination from figure 8 is 0.032, obtained for $\alpha = 0.55$ and $A = 70$. It should be noted here that small values of the inclination angle imply that the stability of the particle against perturbations is small. Any perturbation that is large enough to rotate the particle by an angle of $2((1 + \lambda)/(-2))^{1/2}$ will result in the particle rotating by an angle of π, from one stable equilibrium orientation (near the $+y$-axis) to the other stable equilibrium orientation (near the $-y$-axis).

Typical rigid particle shapes like cylinders, disks, spheroids, and rings with circular cross-section undergoing Jeffery's rotational motion have a period of rotation that increases as the particle becomes thinner, i.e. $\lambda \to \pm 1$ when the particle aspect ratio approaches 0 or ∞. Like ring shapes with circular cross-section, it is the natural

https://doi.org/10.1017/jfm.2013.53 Published online by Cambridge University Press

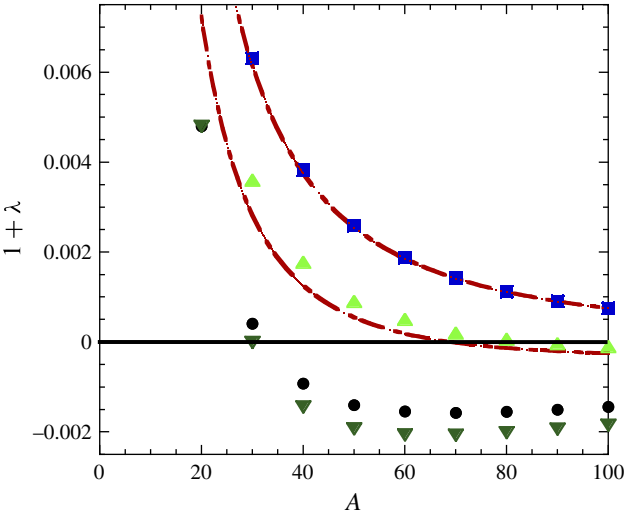


FIGURE 8. (Colour online) Change in the parameter, $1 + \lambda$ (5.5) as a function of non-dimensionalized radius of the ring, A for: □, $\alpha = 0$; △, $\alpha = 0.1$; ○, $\alpha = 0.4$; and ▽, $\alpha = 0.55$. Values of $1 + \lambda$ less than 0 denotes the region where the particle aligns in simple shear flow. The continuous curves for $\alpha = 0$ and 0.1 represent the results from the asymptotic analysis for small α and large A.

tendency of the ring particles with cross-section given by (3.2) to rotate slowly and have small absolute values of $1 + \lambda$ as the aspect ratio is decreased. However, due to the presence of a non-circular cross-section these particles actually stop rotating ($\lambda = -1$) at finite values of the aspect ratio. The transition of the particle from Jeffery-like periodic rotational motion to the aligned state as a function of the particle radius and α is shown in figure 9. Above the curve, particles tumble and below the curve particles do not tumble in the simple shear flow. For the values of α shown in figure 9, the minimum integral value of the radius for which a particle can align is $A = 30$ which occurs for $\alpha \sim 0.55$. The dependence of the maximum flow-aligning aspect ratio on the asymmetry parameter is weak over a broad range $\alpha = 0.4$–0.9 for which the minimum A remains between 30 and 33. This minimum value of the flow-aligning radius is obtained for the cross-sectional shapes studied in this work but probably does not represent the global minimum of the radius (or maximum of the aspect ratio) for all the rigid particle shapes that can align in simple shear flow. For more practical applications of suspensions of these particles, aspect ratio closer to 1 ($A \sim 1$) would be very useful. In this work, we have not attempted to optimize the shape of the cross-section to increase the angular velocity of the particle due to asymmetry. Some of the questions that remain to be answered are: What is the optimum shape of the cross-section which induces maximum angular velocity of the ring due to asymmetry? Are ring-shaped particles the only particles which could align in simple shear flow? If not, then what is the global optimum shape that maximizes the aspect ratio of the non-tumbling particles?

6. Conclusion

In this work, we have presented particle shapes that can stop rotating in simple shear flow. Particles in simple shear flow tumble due to the rotational component of the

https://doi.org/10.1017/jfm.2013.53 Published online by Cambridge University Press

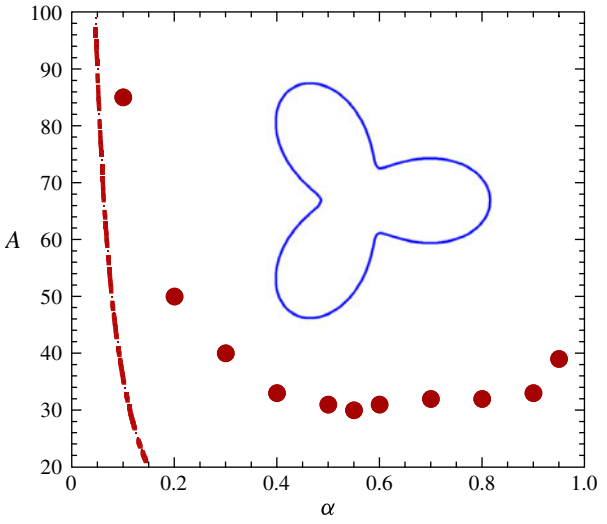


FIGURE 9. (Colour online) State diagram showing the non-dimensionalized radius of the particle at which the particle transitions from a continuously tumbling state to the non-tumbling state for various values of α. The points here represent the smallest integer value of A for which the particle stops tumbling. The cross-sectional shape ($\alpha = 0.55$) of the particle that aligns at a radius of 30 is shown in the graph. The continuous curve represents the transition predicted from the asymptotic analysis in (3.26).

simple shear flow. We have used an asymmetry between the inner and outer portions of a ring cross-section to induce a lateral force per unit length on the cross-section of the particle. The torque due to this force cancels the torque trying to rotate the particle in the vorticity direction at appropriate aspect ratios. The particular shape that we have studied is a ring with the cross-section given by $R = 1 + \alpha \cos 3\beta$ and the radius given by A. Unlike Bretherton's proposed non-tumbling particle shape, the ring-shaped non-tumbling particles do not require a connector and can stop tumbling at finite aspect ratios while maintaining rigidity. To leading order in α, the angular velocity of the particle due to asymmetry is given by $\alpha/2A$. We have shown that lack of fore–aft symmetry of the cross-section is a necessary but not a sufficient condition to induce a lateral force per unit circumference on the particle which is necessary for alignment.

The tumbling parameter for the non-tumbling particle shapes presented in this work lies in the range $\lambda \leqslant -1$ which corresponds to the alignment of axis of symmetry close to the gradient direction, whereas the tumbling parameter of the shape presented by Bretherton (1962*a*) lies in the range $\lambda \geqslant 1$ which corresponds to the alignment of axis of symmetry close to the flow direction. Values of the tumbling parameter for the shapes studied in this work are calculated for different values of A and α. The equilibrium orientation of the axis of symmetry of the particle is found to be close to the gradient direction (figure 8) due to which the stability of the particles to perturbations is not very high. We found that the minimum radius of the ring for which the particle stops rotating is $\sim$30 which is obtained for $\alpha \sim 0.55$.

In the light of the small $1 + \lambda$ values obtained for the non-rotating particle shapes studied here, it is important to examine the practicality of our findings when applied to actual engineering systems. Since most engineering systems would involve Poiseuille

https://doi.org/10.1017/jfm.2013.53 Published online by Cambridge University Press

flows, it is of interest to determine the effect of quadratic flows on the rotational behaviour of the aligning particles. In unbounded quadratic flows, it has been shown that the rotational motion of particles also follows the equation of motion as given by Jeffery (Chwang 1975). Thus even in pipe flow the particles discussed in this work will not undergo rotational motion. In the case of bounded quadratic flow, interactions with the wall also play a role in determining the motion of the particle. There is precedent from the fibre literature which shows that interactions with the wall decreases the rate of rotation of the fibres (Stover & Cohen 1990). Mody & King (2005) have shown that spheroidal disks with $\kappa = 0.25$ when placed beyond a critical distance (1.2 times radius) undergo a retarded Jeffery's rotational motion and at a distance of $\sim$0.7 times the radius completely stop rotating. Thus, for the case of non-rotating rings, it seems likely that wall interactions will not disturb the non-tumbling nature of the particles.

It is possible that hydrodynamic interactions among the particles could lead to tumbling if the asymmetric rings were dispersed in a fluid at finite concentrations rather than as a single particle as considered here. It may be noted however that at very high concentrations steric interactions among Brownian fibres (Chen & Koch 1996) or disks (Jogun & Zukoski 1999) can lead to highly aligned suspensions. It might be expected that steric effects also inhibit rotation at high concentrations in non-Brownian systems. Thus at high concentrations and low concentrations, the non-rotating particles studied here should continue to stay aligned in the flow–vorticity plane. At moderate concentrations the hydrodynamic disturbance of one particle may induce rotation of neighbouring particles. However, even in this case, it seems unlikely that a catastrophic deviation from flow aligning will occur in moderately concentrated suspensions. The velocity disturbance caused by the aligned particles is relatively modest. In addition, if one particle does begin to rotate it is likely to align again after rotating through an angle of π rather than flipping continuously.

Although we have been able to show that the ring-shaped particles can align at moderate aspects ratios of $\sim$30, the physical manifestation of such particles is still going to be challenging. For low Reynolds number and non-Brownian conditions, there is only a small size range, for aspect ratio of 30, in which the particle will continue to align for viscous fluids. The problem of fabrication is further complicated by the kind of shapes (figure 9) needed for alignment at moderate aspect ratio. It seems that a technique like three-dimensional printing can be used to fabricate these particles. For an aspect ratio of 30, one can fabricate a ring with a radius of 1 cm and a cross-section of mean radius 300 μm. For $\alpha = -0.55$, the characteristic length of asymmetry of the cross-section will be 150 μm. This critical dimension is achievable with emerging methods in three-dimensional printing (Lewis 2006). For this size range the particle would not undergo Brownian motion of sufficient amplitude to flip the particle. To achieve low *Re* for this particle size, viscous fluids like glycerine or polybutene (10 Poise) should be used. It should be further noted that in this paper we study cross-sectional shapes with Fourier modes because of the ease of mathematical analysis on such shapes, but cross-sectional shapes like an equilateral triangle and a right-angle triangle should also be able to align the particle at appropriate aspect ratios. These triangular shapes can be fabricated using more conventional fabrication techniques such as lithographic patterning of photosensitive polymers on rigid substrates (Badaire *et al.* 2007). A large number of particles could be formed by replica moulding based on one or a few master structures (Euliss *et al.* 2006). Finally, we note that we have discovered only one class of shape which can

https://doi.org/10.1017/jfm.2013.53 Published online by Cambridge University Press

align, there are possibly other shapes of lower aspect ratio and simpler design which could align and could be fabricated with greater ease.

We will now discuss some broad implications of an aligning particle suspension. The non-rotating nature of the ring-shaped particles discussed in this work can have important rheological consequences on suspensions. In a suspension of rotating circular rings, an $O(\kappa)$ fraction of the rings will be rotating at any given time. These rotating rings experience a force per unit circumference of order $\mu\gamma A^*$ leading to a stresslet, the first moment of the force distribution, of order $\mu\gamma A^{*3}$. Here A^* is the dimensional radius of the ring. The contribution of these rotating rings to the stress in the suspension is $O(n\kappa)$, the number density of flipping rings times their stresslet, yielding an enhancement of the effective viscosity μ_{eff} given by $(\mu_{eff} - \mu)/\mu = O(nA^{*2}c)$ where c is the radius of the ring cross-section. In a suspension of rotating rings, like a suspension of rotating fibres, this contribution from tumbling particles dominates over the contributions from the $O(1)$ fraction of the particles that are near the flow–vorticity plane. In a suspension of non-rotating rings, the particles' contribution to the viscosity is purely due to rings aligned near the flow–vorticity plane which exert an $O(\mu\gamma c^2)$ stresslet per unit circumference on the fluid leading to a much smaller enhancement of the effective viscosity $(\mu_{eff} - \mu)/\mu = O(nA^*c^2)$ than that $(\mu_{eff} - \mu)/\mu = O(nA^{*2}c)$ obtained for rotating rings. Due to this lower resistance to shearing, a suspension of aligning particles could have benefits in terms of ease of processing.

Like the viscosity, the collision rate of ring particles can also be shown to change drastically if the particles do not tumble. For suspensions of tumbling particles with low and high aspect ratio, the leading-order contribution to the collision rate comes from collisions of rotating particles with aligned particles. Following the arguments of Singh *et al.* (2011) for circular cylinders, the leading-order collision rate for a suspension of ring-shaped particle with circular cross-section is given by $O(n^2A^{*2}c\gamma)$. Like thin disks, the contribution to the collision rate from the $O(1)$ fraction of the particles that are near the flow–gradient plane is lower. In a suspension of non-tumbling ring particles there are no particles undergoing rotation, thus the leading-order collision rate arises from collisions of pairs of aligned rings and is given by $O(n^2A^*c^2\gamma)$. This rate is $O(1/A)$ smaller than the collision rate of the rotating ring suspension. A smaller rate of collision would decrease the rate of cluster formation of particles thus improving the processing properties of the suspension.

Materials made from non-tumbling particulate suspensions using methods such as injection moulding could have a high degree of anisotropy because particles will be aligned in a single plane, at least when particle interactions are negligible. As a result the properties of the material such as the elastic modulus, thermal conductivity, magnetic and electric, which depend on the orientation distribution of the constituent material would also be expected to have a high degree of anisotropy. For instance, a thin sheet of composite material containing aligned particles in the flow–vorticity plane during injection moulding could have a high elastic modulus for extensional deformations in the plane of the sheet and a low resistance to shear deformation across the thickness. Similarly, if the particles are highly conducting, the in-plane conductivity of the material could be high and the conductivity across the thickness small. The possibility of tuning material properties in this way motivates further work toward optimizing the shape leading to non-tumbling behaviour and the development of experimental methods to form such non-rotating particles.

https://doi.org/10.1017/jfm.2013.53 Published online by Cambridge University Press

Acknowledgements

We acknowledge support for a graduate fellowship from the Corning Foundation (V.S.), the NYSTAR J.D. Watson Investigator Program, and the National Science Foundation (CTS-0529042).

Appendix

This appendix is divided into two parts. In the first, we solve Stokes flow around the two-dimensional cross-sections of the ring in simple shear flow using the stream-function approach at higher-orders in α. We show that not all cross-sectional shapes which lack fore–aft symmetries can lead to a drift velocity in the gradient direction even at higher-order in α. Thus, while a lack of fore–aft symmetry is a necessary condition to induce a cross-stream velocity, it is not a sufficient condition. In the second part, we simplify the original integral equations by carrying out integrations in the azimuthal direction using complete elliptic integrals, thus transforming the surface integrals into line integrals. Analytical results for the singular integrands encountered in the BEM formulations are also presented.

A.1. *Higher-order drift velocity calculations for a two-dimensional particle lacking fore–aft symmetry*

In § 3 we showed that at leading order in α the cross-stream motion of a two-dimensional particle results only from the third Fourier mode perturbation in shape. However, we might have expected that other odd modes lacking fore–aft symmetry would yield drift at higher-orders in α. It will be shown in this appendix, however that even at higher-orders in α a cross-section described by (3.11) yields cross-stream drift only when $m = 1$. This implies that not all shapes lacking fore–aft symmetry can lead to a non-zero drift velocity. Interestingly, previous studies (Bretherton 1962*a*; Brenner 1964) of asymmetric three-dimensional particles have only considered the third Legendre polynomial and have not commented on the question of whether cross-stream drift occurs, even in the limit of small α, for higher-order mode perturbations in shape.

The general solution for the stream function in simple shear flow around the particle is still given by (3.15) along with the velocity boundary conditions (3.17) and (3.18) on the particle surface. The strategy is again to express the right-hand-side terms in the first boundary condition (3.17) in terms of sine Fourier modes and the second boundary condition (3.18) in terms of cosine modes and then show that even at higher-orders in α only certain modes of the stream function are non-zero. Specifically, we show that shear flow acting on a particle given by (3.11), does not drive $\sin\beta$ or $\cos\beta$ terms in the stream function solution which must be non-zero for a non-zero drift velocity (v_1), unless $m = 1$.

The driving terms for the stream function from the imposed flow in (3.17) and (3.18) are: $R\sin 2\beta$, R and $R\cos 2\beta$. Both the terms $R\sin 2\beta$ and $R\cos 2\beta$ drive the same terms in the stream function solution. Thus we limit our discussion to terms from (3.18) since it has an extra driving term of R from the simple shear flow. Let us now consider a general term from the multipole expansion of the velocity field in (3.18): $\cos(n\beta)/r^{n+1}$. On the surface of the particle, at higher-orders in α this term can be written as:

$$\left.\frac{\cos(n\beta)}{r^{n+1}}\right|_{r=R} = \left(1 - \alpha(n+1)\cos(b\beta) + \alpha^2\frac{(n+1)n}{2}\cos^2(b\beta) - \cdots\cdots\right)\cos(n\beta), \quad \text{(A 1)}$$

https://doi.org/10.1017/jfm.2013.53 Published online by Cambridge University Press

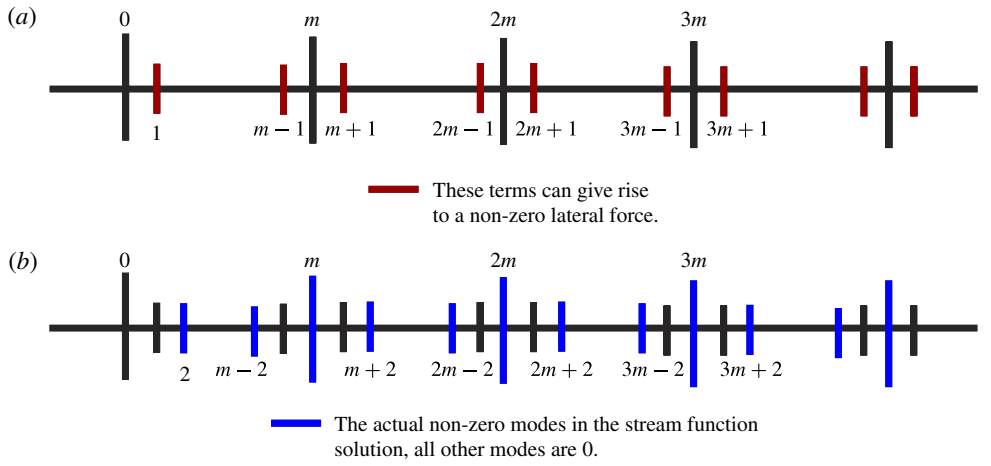


FIGURE 10. (Colour online) (*a*) Fourier modes in the stream function solution that could give rise to a non-zero drift. (*b*) Fourier modes in the stream function solution that are driven by the original shear flow including higher-order terms in the expansion.

where $b = 2m + 1$. To express the above equation in terms of Fourier modes, the product terms, $\cos^a(b\beta)\cos(n\beta)$, can be expressed as summations of cosine terms,

$$\cos(b\beta)\cos(n\beta) = \tfrac{1}{2}(\cos((b+n)\beta) + \cos((b-n)\beta)), \tag{A 2a}$$

$$\cos^2(b\beta)\cos(n\beta) = \tfrac{1}{4}(\cos(2b+n)\beta + 2\cos n\beta + \cos(2b-n)\beta), \tag{A 2b}$$

$$\begin{aligned}\cos^a(b\beta)\cos(n\beta) \rightarrow\ & \cos((ab+n)\beta), \cos(((a-2)b+n)\beta)\ldots \\ & \times \cos((2b+n)\beta), \cos(n\beta), \cos((2b-n)\beta), \ldots \\ & \times \cos((ab-n)\beta), \quad \forall\ \frac{a}{2} \in \mathbb{N},\end{aligned} \tag{A 2c}$$

$$\begin{aligned}\cos^a b\beta \cos n\beta \rightarrow\ & \cos((ab+n)\beta), \cos(((a-2)b+n)\beta)\ldots \\ & \times \cos((b+n)\beta), \cos((b-n)\beta), \ldots \\ & \times \cos((ab-n)\beta), \quad \forall\ \frac{a+1}{2} \in \mathbb{N}.\end{aligned} \tag{A 2d}$$

In the last two results, terms on the left-hand side of the symbol $\rightarrow$ can be written as the sum of the terms on the right-hand side with some pre-factors. These two results can be shown easily using induction. Since a, b and n are non-negative integers, the only terms that can give a $\cos\beta$ term (driving term for the drift velocity) are $\cos((b-n)\beta), \cos((2b-n)\beta), \ldots \cos((ab-n)\beta)$ for $n = b-1, b+1, 2b-1, 2b+1, \ldots ab-1, ab+1$. The Fourier modes in the general solution of the stream function that could give rise to a drift velocity are shown in figure 10(*a*).

Now in order to show that the drift velocity is 0 at higher-orders in α, we need to show that all of the terms in figure 10(*a*) that can give rise to a non-zero drift velocity are zero themselves. This can be proven by showing that all the modes in the stream function driven by the original driving modes of the imposed flow (simple shear flow) are different from the Fourier modes of the general stream function solution (figure 10*a*) that can give a non-zero drift velocity. The original driving modes of simple shear flow in (3.18) are: $\cos(2\beta), \cos(b\beta), \cos((b-2)\beta)$ and $\cos((b+2)\beta)$.

https://doi.org/10.1017/jfm.2013.53 Published online by Cambridge University Press

These original modes can drive the following modes in the stream function solution:

$$\cos^a(b\beta)\cos(2\beta) \to \cos((ab \pm 2)\beta), \quad \cos(((a-2)b \pm 2)\beta)\ldots \tag{A 3a}$$

$$\cos^a(b\beta)\cos(b\beta) \to \cos((ab \pm b)\beta), \quad \cos(((a-2)b \pm b)\beta), \ldots \tag{A 3b}$$

$$\cos^a(b\beta)\cos((b \pm 2)\beta) \to \cos((ab \pm (b \pm 2))\beta), \times \cos(((a-2)b \pm (b \pm 2))\beta), \ldots. \tag{A 3c}$$

In these results again terms on the left-hand side of the symbol $\to$ can be written as the sum of the terms on the right-hand side with some pre-factors. The only Fourier modes in the stream function solution driven by the original modes of simple shear flow are $\pm 2, b, b \pm 2, 2b, 2b \pm 2, \ldots\ldots ab, ab \pm 2$. These modes are represented on the number line in figure 10(*b*) alongside modes that can drive the first Fourier mode. It is clear that there is no overlap between the two sets of modes for $b > 3$. Hence for the cross-sectional shapes given by (3.11), the only shape which will drift in the gradient direction is $m = 1$.

Although within the family of shapes represented by (3.11), only a single shape can undergo drift in the lateral direction, this does not mean that there is only one two-dimensional shape lacking fore–aft symmetry that undergoes drift. Shapes could have a combination of perturbations like:

$$R(\beta) = 1 + \alpha_1 \cos(b_1\beta) + \alpha_2 \cos(b_2\beta) \quad \text{for } b_1, b_2 > 3. \tag{A 4}$$

For these shapes, it can be shown that for a general term $(\cos(n\beta)/r^{n+1}|_R)$ to give a non-zero value of v_1 (or drive the first Fourier mode in the stream function solution): $n = b_1 \pm 1, b_2 \pm 1, b_1 \pm b_2 \pm 1, 2b_1 \pm 1, 2b_2 \pm 1, 2b_1 \pm b_2 \pm 1, b_1 \pm 2b_2 \pm 1, \ldots$. On the other hand Fourier modes of stream function solution driven by the shear flow are: $2, b_1, b_2, b_1 \pm 2, b_2 \pm 2, b_1 \pm b_2 \pm 2, 2b_1, 2b_2, \ldots$.

For a non-zero v_1, there should be a Fourier mode driven by the shear flow that could also drive the first Fourier mode. For $b_1 = 5$ and $b_2 = 7$, one of the Fourier modes of the stream function driven by shear flow is $b_2 + 2 = 9$ and one of the Fourier modes which can drive the first Fourier modes is $2b_1 - 1 = 9$. Thus, this shape can undergo drift in the gradient direction even without the third Fourier mode perturbation in shape. The resultant contribution to the drift velocity is $O(\alpha_1^2\alpha_2)$. For this shape, similarly there is another contribution to drift velocity at $O(\alpha_2^2\alpha_1)$ and other higher-order contributions.

A.2. *Elliptic integral formulations*

Using the azimuthal dependence of stresses from (4.5), the boundary integral equation (4.4) can be written as:

$$\begin{aligned} v_x - y = \int_0^1 \rho'\,\mathrm{d}s'\,\mathrm{d}\theta' (f_1(\rho', y')\cos(2\theta') + f_2(\rho', y')) \left[\frac{1}{(\rho''^2 + (y-y')^2)^{1/2}} \right. \\ \left. + \frac{(\rho\cos\theta - \rho'\cos\theta')^{1/2}}{(\rho''^2 + (y-y')^2)^{3/2}} - \frac{1}{(\rho''^2 + (y+y')^2)^{1/2}} - \frac{(\rho\cos\theta - \rho'\cos\theta')^{1/2}}{(\rho''^2 + (y+y')^2)^{3/2}} \right] \\ + \int_0^1 \rho'\,\mathrm{d}s'\,\mathrm{d}\theta' f_3(\rho', y')\cos(\theta') \left[\frac{(\rho\cos\theta - \rho'\cos\theta')(y-y')}{(\rho''^2 + (y-y')^2)^{3/2}} \right. \\ \left. + \frac{(\rho\cos\theta - \rho'\cos\theta')(y+y')}{(\rho''^2 + (y+y')^2)^{3/2}} \right] \end{aligned}$$

https://doi.org/10.1017/jfm.2013.53 Published online by Cambridge University Press

$$+\int_0^1 \rho'\,\mathrm{d}s'\,\mathrm{d}\theta' f_4(\rho',y')\sin(2\theta')\left[\frac{(\rho\cos\theta-\rho'\cos\theta')(\rho\sin\theta-\rho'\sin\theta')}{(\rho''^2+(y-y')^2)^{3/2}}\right.$$
$$\left.-\frac{(\rho\cos\theta-\rho'\cos\theta')(\rho\sin\theta-\rho'\sin\theta')}{(\rho''^2+(y+y')^2)^{3/2}}\right], \tag{A 5}$$

$$v_y=\int_0^1 \rho'\,\mathrm{d}s'\,\mathrm{d}\theta'(f_1(\rho',y')\cos(2\theta')+f_2(\rho',y'))\left[\frac{(\rho\cos\theta-\rho'\cos\theta')(y-y')}{(\rho''^2+(y-y')^2)^{3/2}}\right.$$
$$\left.-\frac{(\rho\cos\theta-\rho'\cos\theta')(y+y')}{(\rho''^2+(y+y')^2)^{3/2}}\right]+\int_0^1 \rho'\,\mathrm{d}s'\,\mathrm{d}\theta' f_3(\rho',y')\cos(\theta')$$
$$\times\left[\frac{1}{(\rho''^2+(y-y')^2)^{1/2}}+\frac{(y-y')^2}{(\rho''^2+(y-y')^2)^{3/2}}\right.$$
$$\left.+\frac{1}{(\rho''^2+(y+y')^2)^{1/2}}+\frac{(y+y')^2}{(\rho''^2+(y+y')^2)^{3/2}}\right]$$
$$+\int_0^1 \rho'\,\mathrm{d}s'\,\mathrm{d}\theta' f_4(\rho',y')\sin(2\theta')\left[\frac{(\rho\sin\theta-\rho'\sin\theta')(y-y')}{(\rho''^2+(y-y')^2)^{3/2}}\right.$$
$$\left.-\frac{(\rho\sin\theta-\rho'\sin\theta')(y+y')}{(\rho''^2+(y+y')^2)^{3/2}}\right], \tag{A 6}$$

$$v_z=\int_0^1 \rho'\,\mathrm{d}s'\,\mathrm{d}\theta'(f_1(\rho',y')\cos(2\theta')+f_2(\rho',y'))$$
$$\times\left[\frac{(\rho\cos\theta-\rho'\cos\theta')(\rho\sin\theta-\rho'\sin\theta')}{(\rho''^2+(y-y')^2)^{3/2}}\right.$$
$$\left.-\frac{(\rho\cos\theta-\rho'\cos\theta')(\rho\sin\theta-\rho'\sin\theta')}{(\rho''^2+(y+y')^2)^{3/2}}\right]$$
$$+\int_0^1 \rho'\,\mathrm{d}s'\,\mathrm{d}\theta' f_3(\rho',y')\cos(\theta')\left[\frac{(\rho\sin\theta-\rho'\sin\theta')(y-y')}{(\rho''^2+(y-y')^2)^{3/2}}\right.$$
$$\left.+\frac{(\rho\sin\theta-\rho'\sin\theta')(y+y')}{(\rho''^2+(y+y')^2)^{3/2}}\right]+\int_0^1 \rho'\,\mathrm{d}s'\,\mathrm{d}\theta' f_4(\rho',y')\sin(2\theta')$$
$$\times\left[\frac{1}{(\rho''^2+(y-y')^2)^{1/2}}+\frac{(\rho\sin\theta-\rho'\sin\theta')^2}{(\rho''^2+(y-y')^2)^{3/2}}\right.$$
$$\left.-\frac{1}{(\rho''^2+(y+y')^2)^{1/2}}-\frac{(\rho\sin\theta-\rho'\sin\theta')^2}{(\rho''^2+(y+y')^2)^{3/2}}\right], \tag{A 7}$$

where $\rho''=(\rho^2+\rho'^2-2\rho\rho'\cos\theta'')^{1/2}$ is the distance between the two points $\boldsymbol{\rho}$ and $\boldsymbol{\rho}'$ in the ρ–θ-plane, $\theta''=\theta-\theta'$, and $\mathrm{d}s'=\mathrm{d}\rho'\,(1+(\mathrm{d}y'/\mathrm{d}\rho')^2)^{1/2}$ is the arclength. Since the unknowns (f_1,f_2,f_3,f_4) in the above (A 5)–(A 7) are now independent of θ,

https://doi.org/10.1017/jfm.2013.53 Published online by Cambridge University Press

these equations can now be integrated analytically along the azimuthal direction and expressed in terms of complete elliptic functions.

Applying the no-slip boundary condition to the velocity field arising from the boundary-element formulation led to (A 5)–(A 7). The results of integrating (A 5)–(A 7) in the azimuthal direction (θ) can be expressed in terms of complete elliptic integrals. In this subsection, first we express (A 5)–(A 7) in terms of elliptic integrals and then present the asymptotic expansions of the integral to deal with the singularity in the integrand. Rewriting (A 5)–(A 7) we get:

$$(v_x - y)8\pi = I_{xx1} + I_{xx2} + I_{xy} + I_{xz}, \tag{A 8a}$$

$$v_y 8\pi = I_{yx1} + I_{yx2} + I_{yy} + I_{yz}, \tag{A 8b}$$

$$v_z 8\pi = I_{zx1} + I_{zx2} + I_{zy} + I_{zz}, \tag{A 8c}$$

where the integrals on the right-hand side can be defined as:

$$\begin{aligned} I_{xx1} = \int \rho' \,\mathrm{d}s' f_1(\rho')(I_6 + \rho^2\cos^2\theta I_5 + \rho'^2 I_8 - 2\rho\rho'\cos\theta I_7 \\ - I'_6 - \rho^2\cos^2\theta I'_3 - \rho'^2 I'_5 + 2\rho\rho'\cos\theta I'_7), \end{aligned} \tag{A 9a}$$

$$\begin{aligned} I_{xx2} = \int \rho' \,\mathrm{d}s' f_2(\rho')(I_1 + \rho^2\cos^2\theta I_3 + \rho'^2 I_5 - 2\rho\rho'\cos\theta I_4 \\ - I'_1 - \rho^2\cos^2\theta I'_3 - \rho'^2 I'_5 + 2\rho\rho'\cos\theta I'_4), \end{aligned} \tag{A 9b}$$

$$\begin{aligned} I_{xy} = \int \rho' \,\mathrm{d}s' f_3(\rho')(\rho\cos\theta(y - y')I_4 + \rho\cos\theta(y + y') \\ - \rho'(y - y')I_5 - \rho'(y + y')I'_5), \end{aligned} \tag{A 9c}$$

$$\begin{aligned} I_{xz} = \int \rho' \,\mathrm{d}s' f_4(\rho')(2\rho^2\sin\theta\cos\theta I_9 - 2\rho\rho'\sin\theta I_{10} - 2\rho'\rho\cos\theta(I_4 - I_7) \\ + 2\rho'^2(I_5 - I_8) - 2\rho^2\sin\theta\cos\theta I'_9 + 2\rho\rho'\sin\theta I'_{10} \\ + 2\rho'\rho\cos\theta(I'_4 - I'_7) - 2\rho'^2(I'_5 - I'_8)), \end{aligned} \tag{A 9d}$$

$$\begin{aligned} I_{yx1} = \int \rho' \,\mathrm{d}s' f_1(\rho')(\rho\cos\theta(y - y')I_5 - \rho'(y - y')I_7 \\ - \rho\cos\theta(y + y')I'_5 + \rho'(y + y')I'_7), \end{aligned} \tag{A 9e}$$

$$\begin{aligned} I_{yx2} = \int \rho' \,\mathrm{d}s' f_2(\rho')(\rho\cos\theta(y - y')I_3 - \rho'(y - y')I_4 \\ - \rho\cos\theta(y - y')I'_3 + \rho'(y - y')I'_4), \end{aligned} \tag{A 9f}$$

$$I_{yy} = \int \rho' \,\mathrm{d}s' f_3(\rho')(I_2 + (y - y')^2 I_3 + I'_2 + (y + y')^2 I'_3) \tag{A 9g}$$

$$\begin{aligned} I_{yz} = \int \rho' \,\mathrm{d}s' f_4(\rho')(2\rho\sin\theta(y - y')I_9 - 2\rho\sin\theta(y + y')I'_9 \\ - 2\rho'(y - y')(I_4 - I_7) + 2\rho'(y + y')(I'_4 - I'_7)), \end{aligned} \tag{A 9h}$$

$$\begin{aligned} I_{zx1} = \int \rho' \,\mathrm{d}s' f_1(\rho')(\rho^2\sin\theta\cos\theta I_5 - \rho\rho'\cos\theta I_{10} - \rho'\rho\sin\theta I_7 + \rho'^2 I_{11} \\ - \rho^2\sin\theta\cos\theta I'_5 + \rho\rho'\cos\theta I'_{10} + \rho'\rho\sin\theta I_7 + \rho'^2 I'_{11}), \end{aligned} \tag{A 9i}$$

https://doi.org/10.1017/jfm.2013.53 Published online by Cambridge University Press

$$I_{zx2} = \int \rho' \, \mathrm{d}s' f_2(\rho')(\rho^2 \cos\theta \sin\theta I_3 - \rho\rho' \cos\theta I_{12} - \rho'\rho \sin\theta I_4 + \rho'^2 I_9 - \rho^2 \cos\theta \sin\theta I_3' + \rho\rho' \cos\theta I_{12}' + \rho'\rho \sin\theta I_4' - \rho'^2 I_9'), \tag{A 10a}$$

$$I_{zy} = \int \rho' \, \mathrm{d}s' f_3(\rho')(\rho \sin\theta (y - y') I_4 - \rho'(y - y') I_9 + \rho \sin\theta (y + y') I_4' - \rho'(y + y') I_9'), \tag{A 10b}$$

$$I_{zz} = \int \rho' \, \mathrm{d}s' f_4(\rho')(2I_{13} + 2\rho^2 \sin^2\theta I_9 + 2\rho'^2 (I_9 - I_{11}) - 4\rho\rho' \sin\theta (I_4 - I_7) - 2I_{13} - 2\rho^2 \sin^2\theta I_9' - 2\rho'^2 (I_9' - I_{11}') + 4\rho\rho' \sin\theta (I_4' - I_7'))), \tag{A 10c}$$

where I_1–I_{13} are:

$$I_1 = S_1, \tag{A 11a}$$

$$I_2 = \cos\theta S_2, \tag{A 11b}$$

$$I_3 = S_3, \tag{A 11c}$$

$$I_4 = \cos\theta S_4, \tag{A 11d}$$

$$I_5 = \cos(2\theta) S_5 + \sin^2\theta S_3, \tag{A 11e}$$

$$I_6 = (2\cos^2\theta - 1) S_6 + \sin^2\theta S_1, \tag{A 11f}$$

$$I_7 = \frac{3}{4}(\cos\theta - \cos(3\theta)) S_4 + \cos(3\theta) S_7, \tag{A 11g}$$

$$I_8 = \left(\frac{3}{8} - \frac{\cos(2\theta)}{2} + \frac{\cos(4\theta)}{8}\right) S_3 + (\cos(2\theta) - \cos(4\theta)) S_5 + \cos(4\theta) S_8, \tag{A 11h}$$

$$I_9 = \sin(2\theta) S_5 - \frac{\sin(2\theta)}{2} S_3, \tag{A 11i}$$

$$I_{10} = \sin(3\theta) S_7 + \sin\theta (1 - 3\cos^2\theta) S_4, \tag{A 11j}$$

$$I_{11} = \frac{3}{8} \sin(2\theta)(S_5 - S_3) + \frac{\sin\theta}{4}(4\cos(3\theta) S_8 - 3\cos(3\theta) S_5 + 3\cos\theta S_5), \tag{A 11k}$$

$$I_{12} = \sin\theta S_4, \tag{A 11l}$$

$$I_{13} = \sin(2\theta) S_6 - \frac{\sin(2\theta)}{2} S_1 \tag{A 11m}$$

and S_1–S_8 are defined as:

$$S_1 = \int_0^{2\pi} \frac{\mathrm{d}\theta'}{(A_1^2 - B^2 \cos\theta')^{1/2}} = \frac{4}{C_1} K(D_1), \tag{A 12a}$$

$$S_2 = \int_0^{2\pi} \frac{\cos\theta' \, \mathrm{d}\theta'}{(A_1^2 - B^2 \cos\theta')^{1/2}} = \frac{4}{C_1 B^2}(A_2^2 K(D_1) - C_2^2 E(D_2)), \tag{A 12b}$$

$$S_3 = \int_0^{2\pi} \frac{\mathrm{d}\theta'}{(A_1^2 - B^2 \cos\theta')^{3/2}} = \frac{4}{C_1^3} \frac{E(D_1)}{1 - D_1^2}, \tag{A 12c}$$

$$S_4 = \int_0^{2\pi} \frac{\cos\theta' \, \mathrm{d}\theta'}{(A_1^2 - B^2 \cos\theta')^{3/2}} = \frac{4}{C_1^3 B^2} \left(A_1^4 \frac{E(D_1)}{1 - D_1^2}\right), \tag{A 12d}$$

https://doi.org/10.1017/jfm.2013.53 Published online by Cambridge University Press

$$S_5 = \int_0^{2\pi} \frac{\cos^2\theta' \,\mathrm{d}\theta'}{(A_1^2 - B^2\cos\theta')^{3/2}}$$
$$= \frac{4}{C_1^3}\left(\frac{8(D_1^2-2)(D_1^2-1)K(D_1) - 2(D_1^4 - 8D_1^2 + 8)E(D_1)}{2D_1^4(D_1^2-1)}\right), \tag{A 13a}$$

$$S_6 = \int_0^{2\pi} \frac{\cos^2\theta' \,\mathrm{d}\theta'}{(A_1^2 - B^2\cos\theta')^{1/2}}$$
$$= \frac{4}{C_1}\left(\frac{1}{3D_1^4}(4(D_1^2-2)E(D_1) + (3D_1^4 - 8D_1^2 + 8)K(D_1))\right), \tag{A 13b}$$

$$S_7 = \int_0^{2\pi} \frac{\cos^3\theta' \,\mathrm{d}\theta'}{(A_1^2 - B^2\cos\theta')^{3/2}}$$
$$= -\frac{4}{C_1^3}\left(\frac{4(9D_1^6 - 41D_1^4 + 64D_1^2 - 32)K(D_1) - 2(3D_1^6 - 38D_1^4 + 96D_1^2 - 64)E(D_1)}{6D_1^6(D_1^2-1)}\right), \tag{A 13c}$$

$$S_8 = \int_0^{2\pi} \frac{\cos^4\theta' \,\mathrm{d}\theta'}{(A_1^2 - B^2\cos\theta')^{3/2}}$$
$$= \frac{4}{C_1^3}\left(\frac{-2(5D_1^4 - 16D_1^2 + 16)((D_1^4 - 16D_1^2 + 16)E(D_1) - 8(D_1^4 - 3D_1^2 + 2)K(D_1))}{10D_1^8(D_1^2-1)}\right). \tag{A 13d}$$

The first four integrals above are taken directly from Lee & Leal (1982) and the rest are evaluated using the following generic transformation:

$$\int_0^{2\pi} \frac{\cos^a\theta' \,\mathrm{d}\theta'}{(A_1^2 - B^2\cos\theta')^{m/2}} = \frac{(-1)^a 4}{C_1^m}\int_0^{\pi/2} \frac{\cos^a 2\theta' \,\mathrm{d}\theta'}{(1 - D_1^2\sin^2\theta')^{m/2}}. \tag{A 14}$$

The integral on the right-hand side is then evaluated using Mathematica Integrator to give the results in (A 13). Here $A_1 = (\rho^2 + \rho'^2 + (y-y')^2)^{1/2}$, $B = (2\rho\rho')^{1/2}$, $C_1 = (A_1^2 + B^2)^{1/2}$ and $D_1 = (2B^2/(A_1^2 + B^2))^{1/2}$. K and E are complete elliptic integrals given by:

$$K = \int_0^{\pi/2} \frac{\mathrm{d}\theta'}{(1 - D_1^2\sin^2\theta')^{1/2}}, \tag{A 15a}$$

$$E = \int_0^{\pi/2} (1 - D_1^2\sin^2\theta')^{1/2} \,\mathrm{d}\theta'. \tag{A 15b}$$

In the limit $D_1 \to 1$, all the formulae in (A 13) become singular. This condition arises when ρ' approaches ρ and corresponds to calculating the velocity disturbance field very close to a ring of forces. This leads to a weak logarithmic singularity which is integrable. To handle this singularity in the simulations, the integration is performed analytically when $D_1 \to 1$ using the following asymptotic expansions of the elliptic functions (Lee & Leal 1982):

$$K(D_1) = \ln\frac{4}{D_1'} + \frac{1}{2}\left(\ln\frac{4}{D_1'} - 1\right)D_1'^2 + \frac{9}{64}\left(\ln\frac{4}{D_1'} - \frac{7}{6}\right)D_1'^4, \tag{A 16a}$$

https://doi.org/10.1017/jfm.2013.53 Published online by Cambridge University Press

$$E(D_1) = 1 + \frac{1}{2}\left(\ln\frac{4}{D_1'} - \frac{1}{2}\right)D_1'^2 + \frac{3}{16}\left(\ln\frac{4}{D_1'} - \frac{13}{12}\right)D_1'^4, \qquad \text{(A 16}b\text{)}$$

where $D_1' = (1 - D_1)^{1/2}$. The analytical integration is used when $D_1' \leqslant 10^{-6}$. For larger D_1' a numerical integration is performed using complete elliptic integrals.

All the integrals from I_1' to I_{13}' are evaluated in a manner similar to the integrals I_1–I_{13} except A_1 is replaced by $A_2 = (\rho^2 + \rho'^2 + (y + y')^2)^{1/2}$, C_1 by $C_2 = (A_2^2 + B^2)^{1/2}$, and D_1 by $D_2 = (2B^2/(A_2^2 + B^2))^{1/2}$. The integrals I_1'–I_{13}' are not expected to have a singularity because even when $\rho' \to \rho$ the distance between the two points is proportional to the thickness, $2y$.

REFERENCES

BADAIRE, S., COTTIN-BIZONNE, C., WOODY, J. W., YANG, A. & STROOCK, A. D. 2007 Shape selectivity in the assembly of lithographically designed colloidal particles. *J. Am. Chem. Soc* **129**, 40–41.

BATCHELOR, G. K. 1970 Slender-body theory for particles of arbitrary cross-section in Stokes flow. *J. Fluid Mech.* **44**, 419–440.

BHATTACHARYYA, D. S. 1966 Orientation of mineral lineation along the flow direction in rocks. *Tectonophysics* **3**, 559–564.

BRENNER, H. 1964 The Stokes resistance of an arbitrary particle. 3. shear fields. *Chem. Engng Sci.* **19**, 631–651.

BRETHERTON, F. P. 1962*a* The motion of rigid particles in a shear flow at low Reynolds number. *J. Fluid Mech.* **14**, 284–304.

BRETHERTON, F. P. 1962*b* Slow viscous motion round a cylinder in a simple shear. *J. Fluid Mech.* **12**, 591–613.

CHEN, S. B. & KOCH, D. L. 1996 Isotropic-nematic phase transitions in aqueous solutions of weakly charged, rodlike polyelectrolytes. *J. Chem. Phys.* **104** (1), 359–374.

CHEN, S. B. & KOCH, D. L. 1997 Rheology of highly aligned nematic liquid crystals. *J. Non-Newtonian Fluid Mech.* **69**, 273.

CHIEN, S. 1987 Red-cell deformability and its relevance to blood-flow. *Annu. Rev. Physiology* **49**, 177–192.

CHWANG, A. T. 1975 Hydrodynamics of low-Reynolds-number flow. Part 3. Motion of a spheroidal particle in quadratic flows. *J. Fluid Mech.* **72** (1), 17–34.

COX, R. G. 1971 The motion of long slender bodies in a viscous fluid. Part 2. Shear flow. *J. Fluid Mech.* **45** (4), 625–657.

DESCHAMPS, J., KANTSLER, V. & STEINBERG, V. 2009 Phase diagram of single vesicle dynamical states in shear flow. *Phys. Rev. Lett.* **102** (11), 11444–11447.

EDWARDS, D. A., HANES, J., CAPONETTI, G., HRKACH, J., BEN-JEBRIA, A., ESKEW, M. L., MINTZES, J., DEAVER, D., LOTAN, N. & LANGER, R. 1997 Large porous particles for pulmonary drug delivery. *Science* **276** (5320), 1868–1872.

EINSTEIN, A. 1906 Eine neue Bestimmung der Moleküldimensionen. *Ann. Phys. Leipzig* **19**, 289.

EULISS, L. E., DUPONT, J. A., GRATTON, S. & DESIMONE, J. 2006 Imparting size, shape, and composition control of materials for nanomedicine. *Chem. Soc. Rev.* **35**, 1095–1104.

FORGACS, O. L. & MASON, S. G. 1959 Particle motions in sheared suspensions ix. Spin and deformation of threadlike particles. *J. Colloid Sci.* **14**, 457–472.

GAY, N. C. 1967 The motion of rigid particles embedded in a viscous fluid during pure shear deformation of the fluid. *Tectonophysics* **5** (2), 81–88.

GHOSH, S. K. & RAMBERG, H. 1976 Reorientation of inclusions by combination of combination of pure and simple shear. *Tectonophysics* **34**, 1–70.

GOLDSMITH, H. L. 1993 Poiseuille lecture: from papermaking fibers to human red blood cells. *Biorheology* **30**, 165–190.

https://doi.org/10.1017/jfm.2013.53 Published online by Cambridge University Press

GOLDSMITH, H. L. & MASON, S. G. 1962 The flow of suspensions through tubes i. Single spheres, rods, and discs. *J. Colloid Sci.* **17**, 448–476.

GOREN, S. L. & O'NEILL, M. E. 1980 Asymmetric creeping motion of an open torus. *J. Fluid Mech.* **101**, 97–110.

HO, B. P. & LEAL, L. G. 1974 Inertial migration of rigid spheres in two-dimensional unidirectional flows. *J. Fluid Mech.* **65**, 365–400.

HO, B. P. & LEAL, L. G. 1976 Migration of rigid spheres in a 2-dimensional unidirectional shear-flow of a 2nd-order fluid. *J. Fluid Mech.* **76**, 783–799.

ISO, Y., KOCH, D. L. & COHEN, C. 1996 Orientation in simple shear flow of semi-dilute fiber suspensions 2. Highly elastic fluids. *J. Non-Newtonian Fluid Mech.* **62**, 135–153.

JEFFERY, G. B. 1922 The motion of ellipsoidal particles immersed in a viscous fluid. *Proc. R. Soc. Lond.* A **102** (715), 161–179.

JOGUN, S. M. & ZUKOSKI, C. F. 1999 Rheology and microstructure of dense suspensions of plate-shaped colloidal particles. *J. Rheol.* **43** (4), 847–871.

JOHNSON, R. E. & WU, T. Y. 1979 Hydromechanics of low-Reynolds-number flow. Part 5. Motion of a slender torus. *J. Fluid Mech.* **95**, 263–277.

KANTSLER, V. & STEINBERG, V. 2005 Orientation and dynamics of a vesicle in tank-treading motion in shear flow. *Phys. Rev. Lett.* **95** (25).

KIM, S. & KARILLA, S. J. 1991 *Microhydrodynamics*. Dover.

K VEERAPANENI, S., YOUNG, Y.-N., VLAHOVSKA, P. M. & BLAWZDZEIWICZ, J. 2011 Dynamics of a compound vesicle in shear flow. *Phys. Rev. Lett.* **106** (15), 158103.

LADYZHENSKAYA, O. A. 1963 *The Mathematical Theory of Viscous Incompressible Flow*. Gordon and Breach.

LARSON, R. G. 1991 Arrested tumbling in shearing flows of liquid crystal polymers. *Macromolecules* **23**, 3383–3392.

LARSON, R. G. 1999 *The Structure and Rheology of Complex Fluids*. Oxford University Press.

LEAL, L. G. 1980 Particle motion in viscous fluid. *Annu. Rev. Fluid Mech.* **12**, 435–476.

LEAL, L. G. 2007 *Advanced Transport Phenomena*. Cambridge University Press.

LEE, S. H. & LEAL, L. G. 1982 The motion of a sphere in the presence of a deformable interface. ii. a numerical study of the translation of a sphere normal to an interface. *J. Colloid Interface Sci.* **87** (1), 81–106.

LEWIS, J. A. 2006 Direct ink writing of 3d functional materials. *Adv. Funct. Mater.* **16**, 2193–2204.

MODY, N. A. & KING, M. R. 2005 Three-dimensional simulations of a platelet-shaped spheroid near a wall in shear flow. *Phys. Fluids* **17**, 113302.

NIR, A. & ACRIVOS, A. 1973 Creeping motion of 2 arbitrary-sized touching spheres in a linear shear field. *J. Fluid Mech.* **59**, 209–223.

OLLA, P. 1999 Simplified model for red cell dynamics in small blood vessels. *Phys. Rev. Lett.* **82** (2), 453–456.

PELL, W. H. & PAYNE, L. E. 1960 On Stokes flow about a torus. *Mathematika* **7**, 78–92.

POZRIKIDIS, C. 2002 *A Practical Guide to Boundary Element Methods With the Software Library BEMLIB*. Chapman and Hall/CRC.

RAFAI, S., JIBUTI, L. & PEYLA, P. 2010 Effective viscosity of microswimmer suspensions. *Phys. Rev. Lett.* **104**, 098102.

SINGH, V., KOCH, D. L. & STROOCK, A. D. 2011 Ideal rate of collision of cylindrical particles. *Langmuir* **27**, 1813–1823.

SINGH, V., KOCH, D. L., SUBRAMANIAN, G. & STROOCK, A. D. 2013 Rotational motion of a thin axisymmetric disk in a low Reynolds number linear flow. *Phys. Fluids* (in preparation).

STOKES, G. G. 1851 On the effect of the internal friction of fluids on the motion of pendulums. *Cambridge Philos. Trans.* **9**, 8–106.

STOVER, C. A. & COHEN, C. 1990 The motion of rodlike particles in the pressure-driven flow between two flat plates. *Rheol. Acta* **29**, 192–203.

SUBRAMANIAN, G. & KOCH, D. L. 2005 Inertial effects on fibre motion in simple shear flow. *J. Fluid Mech.* **535**, 383–414.

https://doi.org/10.1017/jfm.2013.53 Published online by Cambridge University Press

TCHEN, C. M. 1954 Motion of small particles in skew shape suspended in a viscous liquid. *Am. Inst. Phys.* **25**, 463–473.

THAOKAR, R. M., SCHIESSEL, H. & KULIC, I. M. 2007 Hydrodynamics of a rotating torus. *Eur. Phys. J.* **60**, 325–336.

TORZA, S., COX, R. G. & MASON, S. G. 1972 Particle motions in sheared suspensions xxvii. transient and steady deformation and burst of liquid drops. *J. Colloid Interface Sci.* **38** (2), 396–411.

VASSEUR, P. & COX, R. G. 1976 The lateral migration of a spherical particle in two-dimensional shear flows. *J. Fluid Mech.* **78**, 385–413.

WILLIS, D. G. 1977 Kinematic model of preferred orientation. *Geol. Soc. Am. Bull.* **88** (6), 883–894.

YAMAKAWA, H. & YAMAEI, J. 1973 Application of Kirkwood theory of transport in polymer solutions to rigid assemblies of beads. *J. Chem. Phys.* **58**, 2049–2055.

YOUNGREN, G. K. & ACRIVOS, A. 1975 Stokes flow past a particle of arbitrary shape-numerical-method of solution. *J. Fluid Mech.* **69**, 377–403.

https://doi.org/10.1017/jfm.2013.53 Published online by Cambridge University Press